

promoting access to White Rose research papers



Universities of Leeds, Sheffield and York
<http://eprints.whiterose.ac.uk/>

This is an author produced version of a paper published in **Combustion and Flame**.

White Rose Research Online URL for this paper:

<http://eprints.whiterose.ac.uk/77759/>

Paper:

Bradley, D, Lawes, M, Liao, S and Saat, A (2014) *Laminar mass burning and entrainment velocities and flame instabilities of i-octane, ethanol and hydrous ethanol/air aerosols*. Combustion and Flame (in press).

<http://dx.doi.org/10.1016/j.combustflame.2013.12.0...>

Laminar Mass Burning and Entrainment Velocities and Flame Instabilities of *i*-octane, Ethanol and Hydrous Ethanol/air Aerosols.

D., Bradley¹, M. Lawes¹, S. Y. Liao², A. Saat³

¹School of Mechanical Engineering, University of Leeds, LS2 9JT.

²School of Thermal Engineering, Chongqing University, Chongqing 400044, China.

³Faculty of Mechanical Engineering, Universiti Teknologi Malaysia, 81310, Johor, Malaysia.

E-mail address: d.bradley@leeds.ac.uk (D. Bradley).

Abstract

The paper reports experiments employing the cloud chamber technique for creating fuel aerosols, in studies of premixed laminar flames. Spherical explosion flames were initiated at different times after the start of expansion of the original gaseous mixture to lower pressure. Flame speeds were measured close to atmospheric pressure, over a range of equivalence ratios of *iso*-octane, ethanol and hydrous ethanol with air. A methodology was developed for deriving mass burning velocities and entrainment velocities, as well as mass burning fluxes, from the measurements of aerosol number densities, droplet sizes and flame speeds. It was vital to estimate whether droplet evaporation was completed in the flame preheat zone. This was done by calculating the spatial progress of droplet evaporation for the different aerosols from values of the evaporation rate constants of the different fuels.

With predominantly the leaner mixtures and smaller droplet diameters, evaporation was close to completion, but the mass burning velocities of the aerosols were somewhat lower than those of the corresponding gaseous phases, because of the lower final temperatures due to the required evaporation enthalpies. However, the mass burning fluxes were higher than those for the purely gaseous flames, due to the higher two-phase reactant densities. At the higher values of the liquid phase equivalence ratio, in overall lean mixtures, the mass burning velocity could exceed that in the purely gaseous phase due to localised enrichment around the droplets.

The presence of fuel droplets is shown to enhance the generation of Darrieus-Landau, thermo-diffusive instabilities and the associated flame wrinkling. With richer mixtures and larger droplets, it is possible for droplets to enter the reaction zone and further enhance existing gaseous phase instabilities through the creation of yet further flame wrinkling. This leads to the maximum entrained fuel mass flux, in the richest mixture, being significantly higher than that occurring at the maximum burning velocity of a premixed gaseous flame.

Keywords

Aerosol explosions, flame instabilities, burning velocities, droplet evaporation, hydrous ethanol

Nomenclature

AF_s	molar ratio of air to fuel at stoichiometric condition
B	non-evaporation mass correction factor
D	droplet concentration factor, see Eq. (14)
d	instantaneous droplet diameter
d_{ocr}	critical initial diameter of droplet for 90% evaporation
d_o	initial droplet diameter
k	fuel evaporation rate constant
L_b	flame speed Markstein length
m	total mass within sphere of radius r_f
m_b	mass of burned gas within sphere of radius r_c
m_d	mass of droplets within sphere of radius r_f
m_u	mass of unburned gas within sphere of radius r_f
M_A	molar mass of air
M_F	molar mass of fuel
n	number density of droplets
P	pressure
P_{u0}	initial pressure of mixture
Pe_{cl}	critical Peclet number
R	ratio of r_c / r_f
\bar{R}	universal gas constant
r_c	radius of completely burned zone
r_d	mean radius of droplets
r_f	outer radius of preheat zone
r_{sch}	schlieren flame radius
S	correction factor for flame thickness
S_n	flame speed
S_{no}	flame speed at zero stretch rate
S_{n48}	flame speed at flame radius of 48 mm
T	temperature
T_b	adiabatic flame temperature of burned gas within sphere of radius, r_c
\bar{T}_{uo}	temperature of unburned mixture
\bar{T}_{uT}	mean temperature of unburned gas within sphere of radius, r_f
t	time
u_d	droplet velocity just ahead of the flame
u_g	gas velocity just ahead of the flame
u_e	entrainment velocity at radius, r_f
u_{eg}	entrainment velocity at radius, r_f , for gaseous mixture

u_ℓ	unstretched laminar burning velocity
u_r	mass burning velocity, see Eq. (8)
u_{rg}	mass burning velocity of gaseous mixture

Greek Symbols

ρ	density
ρ_b	density of burned gas within sphere of radius r_c
ρ_d	density of droplets
ρ_{ug}	density of original unburned gas
ρ_{uo}	density of original unburned aerosol
$\overline{\rho_{uT}}$	mean density of unburned gas within sphere of radius, r_f
ϕ	equivalence ratio
ϕ_g	equivalence ratio of gas phase
ϕ_l	equivalence ratio of liquid phase
ξ_p	thickness between start of preheat and the reaction zone, $\xi_p = r_f - r_c$
ν	kinematic viscosity.

1. Introduction

Studies relevant to droplets and spray flames have featured in a number of experimental and numerical investigations for at least seven decades. Such combustion is of practical importance in a wide range of applications including gasoline and diesel engines, gas turbines, and furnaces. The two phase combustion of liquid sprays is usually turbulent, particularly when spray formation occurs in high pressure liquid jets. Because of its practicality, studies of the turbulent combustion of sprays have been more prevalent than those of laminar combustion. The present study concentrates on the measurements of differently defined laminar burning velocities of aerosols and the associated flame instabilities. These are also of fundamental relevance to turbulent burning.

Burgoyne and Cohen [1] generated mono-dispersed liquid aerosols of tetralin in the size range 7 to 55 μm by bubbling heated nitrogen through tetralin. The mixture passed to a re-heater which vaporised the tetralin, following which the mixture passed down a tube, where slow condensation formed a nearly mono-dispersed mist. This was burned in a laminar flame propagating along a tube, and also in a burner. For droplet diameters below 10 μm , combustion was as in the gas phase, while above 40 μm each droplet burned individually in their own envelope of air.

Mizutani and Nakjima [2] measured laminar burning velocities of propane-kerosene droplets-air flames on a burner with an air atomiser and in a cylindrical explosion bomb with an

ultrasonic atomiser [3]. They found that both the burning and propagating velocities of propane flames were markedly accelerated by the addition of a very small amount of kerosene droplets. The smaller they were, the greater the effect. The combustion-promoting effects of droplets were more marked for leaner mixtures and were less so as the mixture became richer than stoichiometric. Polymeropoulos and Das [4] showed that, for kerosene spray flames, with an increasing degree of spray atomization, the flame burning velocity increased to a maximum value, and then decreased to a burning velocity that approached that of the gaseous premixture.

The smaller droplet sizes are better generated by condensation from the gaseous phase, as in a Wilson cloud chamber [5], than by atomisation of the liquid phase. The technique is capable of generating close to monosized droplets in a uniform mixture and was developed for combustion systems by Kumagai and coworkers [6, 7]. Rapid expansion of gaseous ethanol–air mixtures created condensation droplets of ethanol. These might be small enough to vaporise ahead of the reaction zone in a laminar flame, with the fuels initially in a mixture of liquid and gaseous phases. With this technique, Hayashi et al. [7] measured the propagation velocities of ethanol flames through droplets and vapour-air mixtures. Their high quality measurements showed that for a high liquid phase equivalence ratio, ϕ_l , droplets of 4 and 7 μm diameter give a burning velocity less than that of the corresponding homogeneous mixture under lean mixture conditions, but this eventually increased above that of the corresponding gaseous phase mixture for rich mixtures. They also showed, under microgravity conditions, that at sufficiently large flame diameters, cellular flames developed for equivalence ratios, $\phi, > 1.1$. Later experiments [8] showed a tendency of lean aerosol mixtures to burn faster than the corresponding gaseous lean mixture, but the converse occurred for rich mixtures.

Extensive numerical studies by Sirignano [9] and Aggarwal and Sirignano [10] of spray flames showed that the reaction zone does not consist of an array of flames surrounding separate vaporizing droplets, but exhibits, simultaneously, both diffusion-like and premixed-like characteristics. Vaporisation occurs from droplets both behind, and ahead, of the propagating flame. The slip velocity of droplets in the gas flow ahead of the flame causes stratification of the unburned gas mixture and this can lead to an increase in the overall local equivalence ratio ahead of the flame, with a resulting change in the flame speed [10]. Numerical studies of spherical explosive flame propagation with single step Arrhenius kinetics, showed that, as the droplet size increased there were increasing departures from the original uniform equivalence ratio, due to the relative motion of the two phases [11].

Polymeropoulos [12] employed a laminar flame aerosol model with heat release from two sources: single droplet combustion and homogeneous reaction of fuel vapour. He found a

range of droplet sizes, between about 10 and 15 μm , within which the burning velocity was a maximum for both lean and rich mixtures, but there were no conclusive confirmatory experimental observations. Lin and Sheu [13] derived the changes in laminar burning velocities of near-stoichiometric sprays as a function of droplet radius and initial fuel fraction, using matched asymptotics, large activation energy, techniques. For a given droplet radius, the peak value of the burning velocity was displaced to higher values of the overall equivalence ratio by an increase in the liquid fuel fraction.

The combustion modelling of reactive spray in engines by Stapf et al. [14] showed that large droplets create a long trailing vapour cloud with “inferior” ignition and combustion, while the smaller droplet clusters evaporate very quickly generating ignitable fuel-air mixtures.

In their experimental studies of laminar explosions in lean premixed aerosols, Atzler et al. [15] explained the development of relatively low frequency oscillations, accompanied by pulsating flame cellularity, in terms of the droplet slip velocity. The linear stability analyses of Greenberg et al. [16] explain the phenomenon in terms of the heat loss mechanism. Importantly, for richer mixtures, the presence of droplets in the reaction zone creates an energy sink that induces cellular structures, the increased surface area of which increases the burning velocity. In [17] Greenberg developed the evolution equations for the flame and evaporation fronts of a propagating laminar spherical flame, in which the droplets are assumed to vaporise in a sharp front ahead of the reaction front. The dominant influences are the mass fraction of the fuel in the liquid phase and the latent heat of vaporisation of the fuel. Droplets slip velocities are introduced into the equations in [18]. This, and the heat sink arising from droplet evaporation, can cause flame extinction.

Lawes et al. [19] used the cloud chamber technique to generate aerosols just prior to explosion. A phase Doppler anemometer system measured droplet sizes, which increased with time on a scale of seconds. Laminar flame speeds were measured during explosions, from which Markstein numbers were derived. In [20], turbulent burning velocities of aerosols and gases with the same overall ϕ and turbulent parameters were found to be remarkably similar. With laminar combustion the onset of unstable flame cellularity was reached earlier with aerosols, as ϕ was increased, with associated increased burning rates. The progressive introduction of turbulence diminished the influence of the droplets in promoting instability, and the effects of turbulence eventually predominated.

The present experimental work covers measurements of flame speeds in spherical laminar explosions. *Iso*-octane, ethanol and hydrous ethanol mixtures with air were employed. Hydrous ethanol was chosen because bio-ethanol is a possible alternative bio-fuel. A large amount of water is removed in its production by distillation to the azeotropic mixture,

consisting of 3.5% water by volume. To remove all the water requires rather disproportionate amounts of energy, for example, in pumping the mixture through molecular sieves. Consequently, it might be attractive to burn the azeotropic mixture directly in engines, yet there are few data on its burning characteristics.

The thickness of an outer evaporation layer is introduced into a theoretical analysis of different burning velocities. In contrast to previous measurements of flame speed, the present study also evaluates mass burning and entrainment velocities of mixtures into the flame front. In addition, because of their obvious practical and theoretical relevance, the unburned mixture, density-based, mass burning fluxes are found. The nature of instabilities in overall rich flames also is explored. In their review of aerosol explosion hazards, Bowen and Cameron [21] comment on both the inconsistencies in model predictions of laminar burning velocities and the lack of reliable experimental data for their appraisal. The present paper attempts some clarifications in this important area.

2. Experimental Method and Measured Flame Speeds

Ethanol of 99.7% purity, and hydrous ethanol, consisting of the azeotropic mixture, were supplied by Fischer Scientific UK Ltd. *Iso*-octane of 99.9% purity, with 5 ppm maximum water content, was supplied by Ultrafine Ltd.

The gaseous mixture is made up in a cylindrical explosion bomb of 305 mm diameter and 305 mm length and expands along interconnecting pipework into an expansion tank. The expansion rate is controlled by an orifice plate fitted in the loop of pipework. The expansion reduces the pressure and temperature of the mixture in the explosion bomb and when the temperature becomes lower than the saturation temperature of the fuel, condensation occurs and an aerosol cloud is formed. An almost homogeneously distributed suspension of fuel droplets develops within the bomb during the expansion. Initially, their diameter is small, but it can grow to 35 μm .

Mean droplet diameters, d_0 , defined as the simple linear average diameter, were measured using Phase Doppler Anemometry, and the droplet number density, n , by the attenuation of a laser beam and the application of the Beer-Lambert attenuation law. The aerosol parameters were measured in calibration experiments, without combustion, because of the difficulties in measuring droplet size and number density during explosions. After a slow start, up to about 1 ms after the start of expansion, the droplet number density increases rapidly, then slowly declines, whereas d_0 steadily increases, before levelling off. Pressure, P , was measured by a DRUCK PDCR 820 and DP1 280 transducer/readout system, and temperature, T , by K-type thermocouples of 25 μm diameter. Figure 1 shows typical temporal changes in P , T , d_0 , and

n , from a pressure of 0.2 MPa and temperature of 313K at the start of expansion, down to pressures close to 0.1 MPa, for a stoichiometric ethanol-air mixture.

The overall equivalence ratio is given by:

$$\phi = \left(\frac{\text{moles of liquid fuel} + \text{moles of gaseous fuel}}{\text{moles of air}} \right) AF_s = \left(\frac{\text{mass of fuel}}{\text{mass of air}} \right) \left(\frac{M_A}{M_F} \right) AF_s \quad (1)$$

Here AF_s is the mole air/fuel ratio for a stoichiometric mixture and M indicates a molar mass.

ϕ is the sum of the liquid, ϕ_l , and gas, ϕ_g , phase equivalence ratios:

$$\phi = \phi_l + \phi_g. \quad (2)$$

Because the volumetric fraction of the liquid fuel in the mixture is so small compared with the volumes of air and gaseous fuel, the volumetric fraction of the gas phase that is air is given by:

$$\left(\frac{\text{moles of air}}{\text{moles of gaseous fuel} + \text{moles of air}} \right) = \frac{1}{\phi_g / AF_s + 1}. \quad (3)$$

The total mole density of the mixture is $P/\bar{R}T$. Thus the number of air moles in unit volume of the gaseous mixture is $P/\bar{R}T \left(\frac{AF_s}{\phi_g + AF_s} \right)$.

With ϕ_l derived from mass ratios, see the second definition of equivalence ratio in Eq. (1):

$$\phi_l = \left(n\pi\rho_d d_o^3 / 6 \right) \left[M_A P / \bar{R}T \left(\frac{AF_s}{\phi_g + AF_s} \right) \right]^{-1} \left[(M_A / M_F) AF_s \right] \quad (4)$$

$$\phi_l = \left(n\pi\rho_d d_o^3 / 6 \right) \left(\frac{\phi_g + AF_s}{M_F (P/\bar{R}T)} \right) \quad (5)$$

Within the numerator of the second bracketed term, AF_s is dominant and ϕ_l is obtained by iteration, starting with $\phi_g = \phi$ in Eq. (5).

Figure 1 shows the values of ϕ_l derived as discussed above, together with other relevant parameters. The profile in ϕ_l is S-shaped, increasing towards an approximately constant value after about 3 ms from the start of expansion. Different conditions for the same value of ϕ were achieved in two ways. One was to change the initial expansion pressure and to obtain calibration curves, such as those in Fig. 1, during the expansion, The other was to vary the pre-selected instant for ignition during the expansion.

The aerosol mixtures were ignited at the centre of the bomb, at a pre-selected time that depended upon the required aerosol characteristics. A limitation of the technique is the interdependence of d_o and ϕ_l , although these values could be maintained whilst ϕ was varied. The range of conditions that could be covered at different values of ϕ is demonstrated, in the case of *i*-octane/air, in Table 1. More detailed descriptions of the apparatus and associated techniques are given in [15, 19]. Droplet diameters, and their standard deviation, are reported for *i*-octane mixtures at several locations in repeat experiments, within 60 mm of the vessel centre. These showed standard deviations of droplet diameter, due to both cycle to cycle and spatial variations, to be less than 10%. This supports the assumption in the present work that droplets are near mono-dispersed.

The steep rise in n in Fig. 1 is due to the rapid generation of nuclei at the Wilson line. It then decreases from 2.9 to 2.0 m⁻³, a fractional decrease of 0.7. The associated reduction of pressure from 163 to 88 kPa, a fractional decrease of 0.5, expands the volume, whilst the reduction in temperature from 302 to 283K, a fractional decrease of 0.9, compresses it. The net effect is an increase in volume of 0.9/0.5 = 1.8 and a corresponding reduction in n of 1/1.8 = 0.6 on this count. The observed reduction of 0.7 suggests that, during this period, these effects predominated over further droplet nucleation and coalescence. The increase in temperature due to the heat released during condensation contributed to the reduction in n . The continuously increasing values of d_o are probably attributable to increasing condensation around the nuclei with possibly some coalescence. Although the location of the initial condensation sites is stochastic, measurements in both the laser studies and explosions showed good repeatability.

For accurate measurements, the regime of very rapid increase in n on Fig. 1 should be avoided. Thereafter, the values of n were repeatable and accurate. However, whilst the values of n remain fairly steady, those of d_o are changing. Because of the dependency of ϕ_l on d_o^3 , see Eq. (1), the lowest values of ϕ_l are particularly sensitive to these changes. A typical variation of $\pm 10\%$ on diameter measurement for a diameter of 20 μm would give a variation of 18-22 μm and a variation in ϕ_l of 0.08. This gives a liquid equivalence ratio in the region of 0.08 variation of 0.06-0.1, about 50%. The error in the number density is smaller and has much less effect. At later times and higher ϕ_l the effect is less marked.

Similar characteristic curves to those in Fig. 1 were obtained for hydrous ethanol and *i*-octane at different ϕ , again measured by laser attenuation for each mixture. The results suggested that the small amount of water in hydrous ethanol might enhance droplet condensation. The number density showed an approximate increase of 20% and ϕ_l was increased.

During explosions the flame images were captured through the 150 mm diameter windows in the end plates by schlieren cine photography at a framing rate of 3,000 Hz. The flame speed, S_n , was obtained from the rate of increase of flame radius with elapsed time. During the period of an explosion, there was insufficient time for changes in the aerosol parameters. After a propagating flame is established, the spherical flame speed, S_n , is linearly related to the stretch rate, $(2/r)S_n$, at a radius r , until a Darrieus – Landau, or other, flame instability might develop. In this regime, the flame speed at zero stretch rate, S_{no} , is given by:

$$S_n - S_{no} = (2/r)S_n L_b, \quad (6)$$

where L_b is the flame speed Markstein length. The onset of the instability occurs at a critical Peclet number, Pe_{cl} , flame radius normalised by flame thickness given by the kinematic viscosity normalised by the unstretched laminar burning velocity.

Some measured flame speed variations with flame radius are given in Fig. 2. In general, a stretched propagating flame structured became fully developed at a radius of about 25 mm. Thereafter, with the lean mixtures, the flame speed increased slightly as the stretch rate decreased. Figure 2 is for a very rich mixture $\phi = 2.0$, of *i*-octane, with explosions at different values of ϕ_l . As ϕ_l increases with droplet diameter, so does the flame instability and S_n . In order to obtain a near fully developed flame, with minimal stretch rate effects, the studies of burning velocities were made for the larger flame radius of 48 mm, with the flame speed indicated by S_{n48} . As examples, Fig. 3 shows these propagation speeds for (a) ethanol and (b) *i*-octane aerosol/air flames, at different values of ϕ . The full line curves give values for the purely gaseous phase. Other curves are for different combinations of droplet diameter and liquid phase equivalence ratio.

3. Laminar Burning and Entrainment Velocities of Spherical Aerosol Flames

The mass burning velocity, u_r , is the flame velocity relative to the moving unburned mixture ahead of the flame, whereas the flame speed flame speed, S_n , is the observed propagation rate in the laboratory frame of reference. It is not a direct measure of the mass burning rate. To derive this, it is necessary to analyse the explosion in some detail. Consider spherical, explosive, flame propagation through an unconfined homogeneous domain of a mixture of fuel gas, fuel droplets, and air at constant pressure. The mixture domain is characterised by four distinct zones, as shown in Fig. 4. These comprise:

- (i) an outer zone of unreacted mixture in the aerosol cloud,
- (ii) a preheat and droplet evaporation zone,
- (iii) a reaction zone (possibly with some evaporation),

(iv) a burned gas zone at the adiabatic equilibrium temperature of the original mixture.

Zones (ii) and (iii) are separated by the thin fuel consumption layer. The reaction zone of the flame creates a preheat zone ahead of it, within which droplet evaporation occurs. Behind it, reaction proceeds to equilibrated completion. Small droplets might completely evaporate before reacting in the reaction zone. Sufficiently large droplets will survive to burn in a spray, in which case the onset of combustion will rapidly increase the evaporation rate. Any droplet slip velocity is neglected. The effects of this are discussed in Section 6. Finally, combustion is complete. The zone of completely burned gas is of radius, r_c , behind the thin reaction zone. The outer boundary of the preheat zone is r_f . The thickness of the preheat zone, in which evaporation is occurring, is ξ_p (approximated by $r_f - r_c$). The rate of evaporation depends on fuel volatility, latent heat, droplet diameter, and number density. With these assumptions, the total mass within the sphere of radius r_f , m , is made up of the masses of droplets, m_d , (density ρ_d), burned gas, m_b (density ρ_b), and unburned gas m_u (density ρ_u):

$$m = m_d + m_b + m_u, \quad (7)$$

where

$$m_d = n\rho_d \frac{4}{3}\pi(r_f^3 - r_c^3) \frac{4}{3}\pi r_d^3, \text{ and} \quad (8)$$

$$m_b = \frac{4}{3}\pi r_c^3 \rho_b B. \quad (9)$$

Here B is a factor, ≤ 1 , to allow for the possibility that some un-evaporated droplets might coexist in the zone along with the burned gas. Where evaporation is completed ahead of the reaction zone, $B = 1.0$. Even when it is not, reaction is likely to be rapid and B to be less than, but close to, unity. An analysis of droplet evaporation appears in the Appendix. It seeks broadly to identify the regimes in which evaporation is largely completed in the pre-heat zone and in which evaporation is probably continuing in the reaction zone.

With $\bar{\rho}_{uT}$ the mean density of unburned gas (air and fuel vapour) within the sphere of radius, r_f .

$$m_u = \frac{4}{3}\pi(r_f^3 - r_c^3)\bar{\rho}_{uT}(1 - n\frac{4}{3}\pi r_d^3). \quad (10)$$

As droplets evaporate their volume, given by the last term, decreases almost linearly with distance. However for present practical purposes, this can be neglected.

Differentiation of Eq. (9), yields

$$\frac{dm_b}{dt} = 4\pi B r_c^2 \rho_b \frac{dr_c}{dt}. \quad (11)$$

In this analysis, the burning velocity, u_r , is defined by the mass rate of creation of burned gas associated with the area of the sphere of radius r_f , the leading radius of the preheat zone, and the density of the original reactants, ρ_{u0} :

$$\frac{dm_b}{dt} = 4\pi r_f^2 \rho_{u0} u_r. \quad (12)$$

From Eqs. (11) and (12)

$$u_r = B \frac{r_c^2}{r_f^2} \frac{\rho_b}{\rho_{u0}} \frac{dr_c}{dt}. \quad (13)$$

An engulfment or entrainment velocity of both liquid and unburned gas, u_e , also can be defined by the rate of entrainment of the original mixture into the sphere of radius r_f :

$$\frac{dm}{dt} = 4\pi r_f^2 \rho_{u0} u_e \quad (14)$$

From the time differential of Eqs. (7), (8), (10), together with Eqs. (12) and (14):

$$r_f^2 \rho_{u0} u_e = \frac{4}{3} \pi r_d^3 n \rho_d \left(r_f^2 \frac{dr_f}{dt} - r_c^2 \frac{dr_c}{dt} \right) + u_r r_f^3 \rho_{u0} + \left(r_f^2 \frac{dr_f}{dt} - r_c^2 \frac{dr_c}{dt} \right) \bar{\rho}_{u,T} \left(1 - n \frac{4}{3} \pi r_d^3 \right) \quad (15)$$

and

$$u_e = \left(\frac{dr_f}{dt} - \frac{r_c^2}{r_f^2} \frac{dr_c}{dt} \right) \left[\frac{4}{3} \pi r_d^3 n \frac{\rho_d}{\rho_{u0}} + \frac{\bar{\rho}_{u,T}}{\rho_{u0}} \left(1 - n \frac{4}{3} \pi r_d^3 \right) \right] + u_r. \quad (16)$$

Hence

$$u_e - u_r = \left(\frac{dr_f}{dt} - \frac{r_c^2}{r_f^2} \frac{dr_c}{dt} \right) \left[\frac{\bar{\rho}_{u,T}}{\rho_{u0}} + \frac{4n}{3} \pi r_d^3 \frac{\rho_d - \bar{\rho}_{u,T}}{\rho_{u0}} \right]. \quad (17)$$

At the larger flame radii, the conditions approach full development and with sufficient

accuracy $\frac{dr_f}{dt} = \frac{dr_c}{dt}$.

$$\text{Let } R = r_c / r_f = (r_f - \xi_p)^{-1} \text{ and } D = \frac{\bar{\rho}_{u,T}}{\rho_{u0}} + \frac{4n}{3} \pi r_d^3 \frac{\rho_d - \bar{\rho}_{u,T}}{\rho_{u0}}. \quad (18)$$

Consequently,

$$u_e - u_r = \frac{dr_f}{dt} (1 - R^2) D, \quad u_r = BR^2 \frac{\rho_b}{\rho_{u0}} \frac{dr_f}{dt}, \quad \xi_p = r_f (1 - R). \text{ Also } R = 1 - \xi_p / r_f \quad (19)$$

and

$$u_e/u_r = 1 + \frac{(1-R^2)D}{BR^2} \left(\frac{\rho_{uo}}{\rho_b} \right). \quad (20)$$

4. Evaluations of D , R , ρ_{uo}/ρ_b and u_e/u_r

The density of fully burned gas, ρ_b , in the burned zone and the mean density of unburned gas, $\bar{\rho}_{uT}$, in the evaporation and reaction zone are functions of the local temperatures, T_b , and \bar{T}_{uT} respectively. Latent enthalpy is required to evaporate droplets in the original mixture and the adiabatic flame temperature T_b is found by allowing for this evaporation enthalpy. A mean temperature of 1000K is assumed in every case to characterise \bar{T}_{uT} . The density of reactants ρ_{uo} is the mean density of the air, fuel vapour and droplet mixture at the initial conditions. Droplet densities, ρ_d , for total liquid were obtained from the database in [22]. Equation (18) shows the droplet concentration factor, D , to be the sum of the thermal expansion ratio, $\bar{\rho}_{uT}/\rho_{uo}$, and the expansion ratio due to droplet evaporation,

$$\frac{4n}{3} \pi r_d^3 \frac{\rho_d - \bar{\rho}_{uT}}{\rho_{u0}}.$$

Values of D were calculated for all the mixtures explored, with $r_f = 48$ mm for the different experimental values of $d_0 (= 2r_d)$ and n , as well as the appropriate computed densities. Values of $\bar{\rho}_{uT}$ vary only with changes in ϕ , while ρ_{u0} , is affected by the initial temperature, pressure and liquid phase mass fraction. The greater are d_0 and n , the greater is ρ_{u0} , because of the relatively large droplet density. A high value of D indicates a strong direct influence of droplets and, from Eq. (19), higher values of $u_e - u_r$.

The thickness of the preheat zone, ξ_p , is discussed in the Appendix. From the values of ξ_p given in Fig. A2, for different ϕ , R was evaluated at $r_f = 48$ mm, from Eq. (19), and u_e/u_r , with $B=1$, from Eq. (20). In general, the larger values of u_e/u_r were about 1.06, with one excursion to 1.1 with ethanol/air. These larger values occurred with leaner mixtures, as a result of a decrease in values of R , consequent upon the larger values of ξ_p , shown in Fig. A2. For reasons of space, the compiled values of D , R , ρ_{uo}/ρ_b , u_e/u_r , and other parameters, are given in Table 1 only for *i*-octane-air aerosols. These values extend over a greater range of ϕ than those for ethanol and hydrous ethanol. For each value of ϕ , different values of the dependent variables were obtained by changing both the initial expansion

pressure and the instant of ignition. This explains the differing relationships between T_u and P .

The density ratio, ρ_{uo}/ρ_b , is the initial aerosol density divided by the adiabatic burned gas density, with due allowance in the latter value for the latent enthalpy of evaporation. Figure 5 shows such calculated density ratios and adiabatic burned gas temperatures, T_b , for stoichiometric ethanol-air and *i*-octane-air for different liquid phase equivalence ratios, ϕ_l . These and the values for all the other conditions were obtained using the GasEq code [23]. It can be seen that burned gas temperatures decrease with increasing ϕ_l . This is because of the required latent enthalpy of evaporation, which is about three times greater for ethanol than for *i*-octane. Values of ρ_{uo}/ρ_b increase with ϕ , due to the greater density of droplets, dominating over the increase in ρ_b due to the required latent enthalpy.

It is of interest to note from Table 1 that, for a flame radius of 48 mm, values of R^2 range between 0.97 and 0.99. The range of values of D , expressing the role of droplets, is larger, from 0.22 to 0.27. The higher values of ϕ_l are associated with the higher values of D , as well as maximum values of $D/(\bar{\rho}_{uT}/\rho_{u0})$, showing the dominance of the effect of droplet mass.

5. Mass Burning Velocities, Entrainment Velocities, and Critical Peclet Numbers

For the purely gaseous mixtures ($d_0 = 0$ and $\phi_l = 0$), the corresponding burning velocities, indicated by u_{rg} and u_{eg} , are related to measured flame speeds, S_n , by the expressions derived in [24] for similar conditions. For the aerosols, Eqs. (19) were used to derive u_r and u_e . The starting point is the values of $dr_f/dt = dr_{sch}/dt$, at a radius of 48 mm, and given by S_{n48} in Fig. 3 for ethanol/air and *i*-octane/air. Figure 6 shows the derived respective mass burning velocities, u_r , for (a) ethanol-air and (b) *i*-octane-air, plotted for the different values of d_0 and ϕ_l .

The differences between dry and hydrous burning of ethanol are explored in Fig. 7, in which (a) compares their gaseous flame speeds and (b) their mass burning velocities. Full line curves give dry ethanol values and dotted curves hydrous values. The effects of different hydrous ethanol droplet sizes on flame speeds and mass burning velocities also are shown. The overall equivalence ratio, ϕ , was defined in terms of the fuel/air mole ratio, with pure ethanol as the fuel, and water as a diluent. For the same conditions as Fig. 3, Fig. 8 shows the entrainment velocities, u_e , while Fig. 9 shows these for the conditions of Fig. 7.

With $\phi = 1.2$ there was no marked cellular instability [25, 26] on the schlieren images of gaseous *i*-octane and ethanol flames. There were signs of cells developing, with $d_o = 5$ and $12 \mu\text{m}$, but less so for greater values of d_o . For *i*-octane, however, increases in ϕ beyond 1.2 led to the development in cellularity for all flames. In general, it was found that the critical Peclet number, Pe_{cl} , for the onset of flame instabilities in purely gaseous mixtures was decreased by the presence of droplets of increasing size, as shown by the plots of Pe_{cl} for different droplet diameters in four *i*-octane/air aerosol mixtures in Fig. 10.

Because of the presence of a reactant liquid phase, mass burning and entrainment fluxes were greater than those for the same gaseous mixtures. These were obtained per unit area of the leading surface at r_f , by multiplying both u_r and u_e by the density of the reactants, ρ_{uo} . Values of $\rho_{uo}u_r$, at different ϕ , for the three fuels are shown in Figs. 11 – 12. Values for the gaseous phase are again shown by full line or, in the case of hydrous ethanol, dotted curves.

6. Discussion of Experimental Results

Oscillatory regime

The extent of droplet vaporisation in the preheat zone influences the flame structure and burning velocities, u_r , of aerosol flames and their relationships to those of the equivalent gaseous flames, u_{rg} . At very low values of ϕ and the larger droplet sizes this interaction can induce low frequency flame oscillations. Measurements of these are reported and the phenomenon discussed in [15]. This has been explained by measurements of oscillatory flame speeds, S_n , and droplet velocities, u_d , in [15]. As the flame accelerates from its original kernel, the drag on the droplets decreases their velocity, u_d , to below that of the gas, u_g . This creates a region just ahead of the flame, of increased ϕ_l .

As the flame moves into this enriched mixture both S_n and u_g increase. The richer mixture might become unstable and cellular, further increasing these parameters. When the flame has passed through this enriched region, the values of S_n and u_g fall, and the cellularity disappears. Because of the slower retardation of the droplets, u_d , becomes greater than u_g . This creates a region ahead of the flame with an increased ϕ_l , the flame accelerates and the cycle is repeated. This effect is enhanced by a high slip velocity, high ϕ_l , and the large changes in flame speed with ϕ that occur with lean mixtures. Droplet velocities ahead of the flame fluctuate about a mean value, as does the flame speed. The mean flame speed is close to the value that would have been expected in the absence of oscillations. In the present work oscillations developed in the ethanol flames of Fig. 6(a) at $\phi = 0.7$, when the initial droplet

diameter was increased above 12 μm . Although interesting, the oscillatory regime was avoided and not studied further in the present work.

High evaporation in preheat zone, $d_o \leq 14 \mu\text{m}$

It is instructive, in revealing something of the nature of aerosol flames, to normalise mass burning velocities by those of the equivalent gaseous mixture. Such ratios of u_r/u_{rg} are presented for the three fuels in Figs. 13 and 14. The smallest droplets, with $d_o = 5, 12,$ and $14 \mu\text{m}$, would, according to Fig. A2, be more than 90% evaporated for values of ϕ up to 1.2, for all three fuels. Because of this, u_r might be expected to be close to u_{rg} ,

Figures 6, 7, 13 and 14 tend to confirm that this is approximately so. However, there is a tendency over these ranges for u_r , although less than u_{rg} , to be closer to it in the case of *i*-octane, than in the case of ethanol, for which u_r/u_{rg} was generally smaller. This is explained by the greater enthalpy of evaporation and greater lowering of T_b with ethanol than with *i*-octane in Fig. 5. The further lowering of T_b with hydrous ethanol at the same ϕ results in an increasing lowering of u_{rg} values, below those for ethanol, with increasing ϕ .

Because of the higher density of aerosols compared to gaseous, reactants, with the exception of those aerosols with very small droplet diameters, the mass burning fluxes increased with ϕ_l in this range, as can be seen from Figs. 11 and 12.

Low evaporation in preheat zone and ultimate flame quenching $d_o \geq 20 \mu\text{m}$

In contrast, at the larger droplet sizes of 31 μm for ethanol and 20 μm for *i*-octane at $\phi = 0.8$, with less than 90% evaporation in the preheat zone, it is striking, particularly for hydrous ethanol, that Figs. 6, 7, 13 and 14 show enhanced mass burning velocities, now with $u_r > u_{rg}$. With an increasing proportion of droplets entering the reaction zone as ϕ increases, B would decrease slightly, as also would u_r . As suggested by Nomura et al. [8], it would seem that the un-evaporated droplets might subsequently burn more rapidly in localised fuel-enriched regions within a lean environment, with a resulting increase in u_r . However, for all the richer mixtures with $\phi = 1.0$ and 1.2, at the highest values of d_o and ϕ_l for each fuel, and for which Fig. A2 suggests evaporation is even less complete, Figs. 13 and 14 suggest u_r is significantly less than u_{rg} . Indeed at $\phi = 1.2$ there is a tendency for flame quenching to develop, particularly for *i*-octane, as indicated in Fig. 15. This figure shows mass burning and mass entrainment fluxes, normalised by the mass burning fluxes of the equivalent gaseous flames, plotted against ϕ_l . Such enhancements and reductions also occurred in the ethanol flame speeds measured in [8] at $\phi_l = 0.3$.

Figure 15 shows the effects of an increase in ϕ_l on the normalised mass burning fluxes, at four different values of ϕ_l for both fuels. The approach towards eventual flame extinction with increasing ϕ_l is well demonstrated by the decline in normalised mass burning fluxes at $\phi = 1.2$ for both ethanol and *i*-octane. The theoretical analysis of Greenberg [18] has expressed this tendency towards flame extinction in terms of a vaporisation Damköhler number. He showed droplet drag can induce extinctions due to the longer residence time of the droplets. This increases with vaporisation of droplets and the heat loss term in the flame front evolution equation, which is proportional to ϕ_l . The present study concentrates on aerosol flames and the measurement of extinction limits was not pursued further.

Rich flames with evaporation in reaction zone

The *i*-octane characteristics in Fig. 15(b) indicate that flame quenching can be avoided and ϕ_l further increased if ϕ is increased. Furthermore, as indicated also on Figs. 6(b) and 13(b), strikingly high values of u_r/u_{rg} , of up to 3.1, can be attained at $\phi = 2.0$ at the largest ϕ_l . Extrapolations of the *i*-octane curve on Fig. A2 suggests for those flames with $d_o = 20, 18$ and probably $14 \mu\text{m}$ on Figs. 6(b) and 13(b), the droplets would be less than 90% evaporated in the preheat zone. Perhaps for $d_o = 5 \mu\text{m}$ the droplets would always be at least 90% evaporated. As ϕ is increased above 1.2, up to $\phi = 2.0$, gaseous flames experience increasing Darrieus-Landau, thermo-diffusive, instabilities that are reflected in increased values of u_{rg} . Figures 6(b) and 13(b) show further increases in u_r and in u_r/u_{rg} with ϕ , for all values of d_o greater than $5 \mu\text{m}$. This suggests the generation of strong additional instabilities with increasing d_o and the presence of droplets in the reaction zone. This is without any reduction in u_r , despite the associated decrease in the B factor. That the presence of droplets further enhances the onset of cellular instabilities is shown by the lowering of the critical Peclet number, Pe_{cl} , when d_o and ϕ are increased on Fig. 10.

Such an additional instability in rich spray flames, beyond that in purely gaseous flames, has been explained by Greenberg et al. [16] by the presence of vaporising droplets inside the reaction zone. These create further cellular structures that are not present in the absence of droplets. Because of this, the degree of cellularity in a rich flame is much greater than that in the equivalent cellular gaseous flame. The increase in flame surface area increases the burning velocity. It is noteworthy that in Figs. 6(b) and 13(b), for $\phi > 1.2$ and $d_o = 5 \mu\text{m}$, and with Fig. A2 suggesting evaporation is probably completed within the preheat zone, there is but

small enhancement of u_r . Interestingly, the addition of water droplets to a propane-air flame at $\phi = 1.3$, enhanced cellularity, whilst decreasing the flame speed [27].

An important aspect of this increased instability is the increased entrainment of fuel into the flame. This is demonstrated by the mass entrainment fluxes of ethanol/air and *i*-octane flames at different ϕ , normalised by the mass burning fluxes of the equivalent gaseous flames, shown in Fig. 16. Curves are given for different droplet characteristics. The ratio of normalised entrainment flux reaches as high as almost 3.5 for the largest droplet diameter and liquid phase equivalence ratio in the *i*-octane flame with $\phi = 2.0$. The variations of mass entrainment fluxes with ϕ in Fig. 17 show the maximum value at $\phi = 2.0$ is higher than the maximum for a purely gaseous flame, which occurs at $\phi = 1.3$. The mass fraction of fuel is greater in the aerosol mixture at $\phi = 2.0$, and it can readily be shown that the mass flux of fuel is 50% greater with $\phi_l = 0.30$ in this most unstable aerosol, than it is in the maximum mass flux in a gaseous flame.

7. Conclusions

The cloud chamber method of producing fuel aerosols for combustion studies has been shown to be valuable in highlighting the leading characteristics of aerosol flames. This is despite the droplet diameter and number density not being controlled independently in the present work. In spite of some uncertainties in values of evaporation rate constants for ethanol, hydrous ethanol, and *i*-octane, it was possible to make reasonable estimates of the relative amount of evaporation that had occurred ahead of the reaction zone.

In addition to measuring aerosol and gaseous flame speeds, the present study, unlike previous ones, has derived from these, mass burning and reactant entrainment velocities. Mass burning fluxes also were obtained, allowing for the two phase nature of the reactants. With predominantly lean mixtures and smaller droplet diameters, the mass burning velocities of the aerosols were somewhat lower than those of the corresponding gaseous phases, on account of the lower final temperatures due to the required evaporation enthalpies. In contrast, the mass burning fluxes tended to be higher than those for the purely gaseous flames, due to the higher two phase reactant densities.

As ϕ_l and d_o increase, evaporation becomes less complete in the preheat zone. For lean mixtures this can lead to increases in u_r above u_{rg} as localised enrichment around droplets increases u_r . However, for $\phi = 1.2$, there was evidence that further increases in ϕ_l would eventually quench the combustion.

The presence of fuel droplets at a given value of ϕ enhances the generation of Darrieus-Landau, thermo-diffusive, instabilities and the associated flame wrinkling. It also decreases the critical Peclet number for their onset. More fundamentally, this represents an increase in the value of the critical Karlovitz stretch factor, below which instabilities develop [26]. A striking aspect of the work is that when droplets enter the reaction zone of rich mixtures existing instabilities of this type are further enhanced by the creation of yet further wrinkling. This leads to significant increases in u_r above u_{rg} . Because of this effect, the overall maximum measured entrainment mass flux occurs with the largest values of ϕ_l and d_o , at the largest equivalence ratio of 2.0, in *i*-octane/air. The maximum mass flux of entrained fuel is 50% greater for this highly unstable aerosol flame than for the purely gaseous flame at its maximum burning velocity. This is of some relevance to the hazards posed by the release of flammable vapour clouds. It must, however be recalled, that turbulence can override such aerosol instabilities [20], just as it can override laminar instabilities in purely gaseous flames [28].

The data for hydrous ethanol as a practical fuel suggest that its gas phase burning velocity is somewhat less than that of ethanol, particularly at the higher values of ϕ . The various observed two phase effects seem to be slightly enhanced with hydrous ethanol.

References

1. J.H. Burgoyne, L. Cohen, (1954) Proc. Roy. Soc. A225, 375-392.
2. Y. Mizutani, A. Nakajima, (1973) Combust. Flame 20, 343-350.
3. Y. Mizutani, A. Nakajima, (1973) Combust. Flame 20, 351-357.
4. C.E. Polymeropoulos, S. Das, (1975) Combust. Flame 25, 247-257.
5. C.T.R. Wilson, (1911) Proc. Roy. Soc. London Ser. A85, 285-288.
6. S. Hayashi, S. Kumagai, (1975) Proc. Combust. Inst. 15, 445-452.
7. S. Hayashi, S. Kumagai S., T. Sakai, (1976) Combust. Sci. and Tech. 15, 169-177.
8. H. Nomura, M. Koyama, H. Miyamoto, Y. Ujiie, J. Sato, M. Kono, S. Yoda, (2000) Proc. Combust. Inst. 28, 999-1005.
9. W.A. Sirignano, (1983) Prog. Energy Combust. Sci. 9, 291-322.
10. S.K. Aggarwal, W.A. Sirignano, (1985) Combust. Flame 121, 181-194.
11. G. Continillo, W.A. Sirignano, (1988) 22nd Symposium (Int.) on Combustion, 1941-1949.
12. C.E. Polymeropoulos, (1984) Combust. Sci. Tech. 40, 217-232.
13. T.H. Lin, Y.Y. Sheu, (1991) Combust. Flame 84, 333-342.
14. P. Stapf, H.A. Dwyer, R.R. Maly, (1998) Proc. Combust. Inst. 27, 1857-1864.
15. F. Atzler, F.X. Demoulin, M. Lawes, Y. Lee, N. Marquez, (2006) Combust. Sci. and Tech. 178, 2177-2198.
16. J.B. Greenberg, A.C. McIntosh, J. Brindley, (2001) Proc. Roy. Soc. A457, 1-31.
17. J.B. Greenberg, (2003) Combust. Theory and Modelling 7, 163-174.
18. J.B. Greenberg (2007) Combust. Flame 148, 187-197.
19. M. Lawes, Y. Lee, N. Marquez, (2006) Combust. Flame 144, 513-525.
20. M. Lawes, A. Saat, (2011) Proc. Combust. Inst. 33, 2047-2054.
21. P.J. Bowen, L.R.J. Cameron, (1999) Institution of Chemical Engineers Trans IChemE, 77 Part B, 22-30.
22. Liquids - Densities. http://www.engineeringtoolbox.com/liquids-densities-d_743.html (accessed 12.09.2011).
23. C. Morley, (2012) Gaseq Chemical Equilibrium Program. Available from c.morley@ukgateway.net
24. D. Bradley, P.H. Gaskell, X.J. Gu, (1996) Combust. Flame 104, 176-198.
25. D. Bradley, C.G.W. Sheppard, R. Woolley, D.A. Greenhalgh, R.D. Locket, (2000) Combust. Flame 122, 195-209.
26. D. Bradley, M., Lawes, M.S. Mansour, (2009) Combust. Flame 156, 1462-1470.
27. F. Atzler, (1999) "Fundamental studies of aerosol combustion", PhD thesis, School of Mechanical Engineering, University of Leeds, Leeds, UK.
28. D. Bradley, M. Lawes, Kexin Liu, M.S. Mansour, (2013) Proc. Combust. Inst. 34, 1519-1526.

Table and Figure Captions

Table 1. Measurements with experimental conditions and computed D and R ($r_f = 48$ mm) for : i -octane/air.

Table A1. Evaporation rate constants for ethanol, and i -octane, and n -octane.

Figure 1. Typical variation of aerosol characterisation with the time for stoichiometric ethanol-air mixture expanded from 200 kPa, 313K.

Figure 2. Variations of flame speeds at atmospheric pressure and temperature with radius for gaseous and aerosol iso -octane-air mixtures at $\phi = 2.0$, for different droplet diameters and liquid phase equivalence ratios, ϕ_l .

Figure 3. Flame propagating speeds of (a) ethanol/air and (b) i -octane/air flames at a radius of 48 mm, flames with various droplet sizes and liquid equivalence ratios.

Figure 4. Spherically expanding aerosol flame configuration. , with evaporation completed in the preheat zone.

Figure 5. Variations, due to droplets, of burned gas temperature and ratio of densities for stoichiometric ethanol and i -octane aerosol mixtures.

Figure 6. Mass burning velocities of (a) ethanol/air and (b) i -octane flames in air, at a radius of 48 mm with different droplet characteristics.

Figure 7. (a) Flame propagation speeds of hydrous ethanol/air and ethanol/air for different droplet characteristics. (b) Mass burning velocities of hydrous ethanol/air flames, at a radius of 48 mm with different droplet characteristics. Gaseous phase values on both (a) and (b).

Figure 8. Entrainment velocities of ethanol and i -octane flames, at a radius of 48 mm with different droplet characteristics.

Figure 9 Entrainment velocities of hydrous ethanol/air flames, at a radius of 48 mm with different droplet characteristics.

Figure 10. Variations of Pe_{cl} with d_o at different ϕ for i -octane/air aerosol flames.

Figure 11. Mass burning fluxes of ethanol and i -octane/air flames with different droplet characteristics.

Figure 12. Mass burning fluxes of hydrous ethanol/air flames with different droplet characteristics.

Figure 13. Normalised mass burning velocities of ethanol and i -octane/air /flames, with different droplet characteristics.

Figure 14. Normalised mass burning velocities of hydrous ethanol and ethanol/air flames, with different droplet characteristics.

Figure 15. Effects of liquid equivalence ratio on mass burning and mass entrainment fluxes, normalised by the mass burning fluxes of the equivalent gaseous flames. The droplets diameters are 0, 5, 12, 23 and 31 μm for ethanol/air mixtures and 0, 5, 14, 18 and 20 μm for i -octane with increasing ϕ_l respectively.

.Figure 16. Normalised mass entrainment fluxes of ethanol/air and i -octane flames with different droplet characteristics.

Figure 17. Mass entrainment fluxes of i -octane flames with different droplet characteristics.

Figure A1. Some calculated changing droplet diameters due to evaporation in preheat zone, thickness, ξ_p , for ethanol/air mixtures.

Figure A2. Critical initial droplet diameters, d_{ocr} , for 90% evaporation in preheat zone, thickness ξ_p , at different ϕ for ethanol/air and *i*-octane/air. Asterisks suggest values given by flame speeds.

Table 1. Measurements with experimental conditions and computed D and R ($r_f = 48$ mm) for : i -octane/air.

ϕ	ϕ_l	P (MPa)	T_u (K)	T_b (K)	d_0 (μm)	$n \times 10^9$ (m^{-3})	ρ_{uo} (kg/m^3)	ρ_b (kg/m^3)	$\bar{\rho}_{uT}$ (kg/m^3)	$\frac{\rho_{uo}}{\rho_b}$	$\frac{\bar{\rho}_{uT}}{\rho_{u0}}$	D	R^2	u_e/u_r ($B=1$)
0.8	0	0.120	276	2038	0	0	1.557	0.201	0.410	7.734	---	---	---	---
0.8	0.001	0.121	271	2034	5	1.7	1.599	0.203	0.414	7.866	0.259	0.259	0.975	1.052
0.8	0.229	0.093	263	2022	20	6.4	1.286	0.157	0.318	8.166	0.247	0.264	0.971	1.064
0.9	0.000	0.097	279	2177	0	0	1.249	0.152	0.330	8.240	---	---	---	---
0.9	0.004	0.093	278	2176	5	7.2	1.202	0.145	0.317	8.267	0.263	0.264	0.976	1.054
0.9	0.118	0.097	277	2174	14	9.5	1.268	0.152	0.330	8.345	0.260	0.269	0.977	1.053
0.9	0.243	0.094	265	2164	20	6.8	1.295	0.148	0.320	8.750	0.247	0.264	0.976	1.055
1.0	0	0.097	278	2265	0	0	1.258	0.145	0.328	8.700	---	---	---	---
1.0	0.004	0.095	277	2264	5	7.2	1.237	0.142	0.321	8.729	0.259	0.260	0.979	1.048
1.0	0.035	0.089	272	2259	10	7.2	1.183	0.133	0.301	8.888	0.254	0.257	0.978	1.051
1.0	0.127	0.099	278	2263	14	10.0	1.294	0.148	0.334	8.758	0.258	0.267	0.980	1.049
1.0	0.215	0.099	273	2259	18	8.4	1.326	0.148	0.334	8.953	0.252	0.267	0.979	1.051
1.0	0.244	0.096	268	2255	20	6.9	1.313	0.144	0.324	9.122	0.247	0.264	0.978	1.053
1.1	0	0.097	279	2265	0	0	1.258	0.143	0.323	8.827	---	---	---	---
1.1	0.125	0.102	278	2263	14	10.0	1.338	0.150	0.340	8.915	0.254	0.263	0.983	1.042
1.1	0.337	0.098	270	2254	20	9.6	1.343	0.145	0.326	9.271	0.243	0.266	0.981	1.047
1.2	0	0.100	280	2203	0	0	1.297	0.148	0.327	8.743	---	---	---	---
1.2	0.004	0.100	280	2202	5	7.6	1.297	0.148	0.327	8.745	0.252	0.252	0.984	1.037
1.2	0.036	0.093	275	2198	10	7.5	1.231	0.138	0.304	8.904	0.249	0.249	0.983	1.037
1.2	0.128	0.105	279	2200	14	11.0	1.378	0.156	0.343	8.834	0.249	0.258	0.985	1.034
1.2	0.293	0.103	270	2191	18	12.0	1.412	0.154	0.337	9.184	0.238	0.259	0.985	1.036
1.2	0.332	0.100	271	2191	20	9.6	1.369	0.149	0.327	9.172	0.239	0.262	0.981	1.046
1.4	0	0.108	283	2050	0	0	1.395	0.166	0.340	8.425	---	---	---	---
1.4	0.004	0.105	282	2050	5	7.6	1.361	0.161	0.330	8.454	0.242	0.243	0.985	1.032
1.4	0.125	0.110	281	2047	14	11.0	1.442	0.169	0.346	8.536	0.240	0.249	0.987	1.029
1.4	0.365	0.108	276	2040	18	15.0	1.464	0.167	0.340	8.787	0.232	0.257	0.985	1.033
1.4	0.475	0.104	275	2038	20	14.0	1.425	0.161	0.327	8.872	0.229	0.262	0.984	1.037
1.6	0	0.111	285	1903	0	0	1.433	0.177	0.336	8.109	---	---	---	---
1.6	0.004	0.111	285	1903	5	7.2	1.433	0.177	0.336	8.111	0.235	0.235	0.982	1.035
1.6	0.033	0.103	283	1901	10	7.5	1.342	0.164	0.312	8.175	0.233	0.235	0.983	1.033
1.6	0.121	0.116	283	1900	14	11.0	1.519	0.185	0.351	8.212	0.231	0.240	0.986	1.028
1.6	0.372	0.113	279	1894	18	16.0	1.525	0.181	0.342	8.432	0.224	0.250	0.985	1.031
1.6	0.503	0.109	278	1892	20	15.0	1.488	0.175	0.330	8.516	0.222	0.256	0.984	1.035
2.0	0	0.125	293	1637	0	0	1.589	0.216	0.354	7.356	---	---	---	---
2.0	0.003	0.122	290	1635	5	6.0	1.567	0.211	0.345	7.424	0.220	0.220	0.964	1.062
2.0	0.027	0.115	286	1631	10	6.8	1.500	0.199	0.325	7.524	0.217	0.219	0.973	1.045
2.0	0.112	0.123	286	1631	14	11.0	1.613	0.213	0.348	7.558	0.216	0.223	0.981	1.033
2.0	0.272	0.112	283	1627	18	12.0	1.500	0.195	0.317	7.699	0.211	0.230	0.980	1.035
2.0	0.500	0.125	282	1624	20	17.0	1.703	0.218	0.354	7.813	0.208	0.241	0.985	1.028

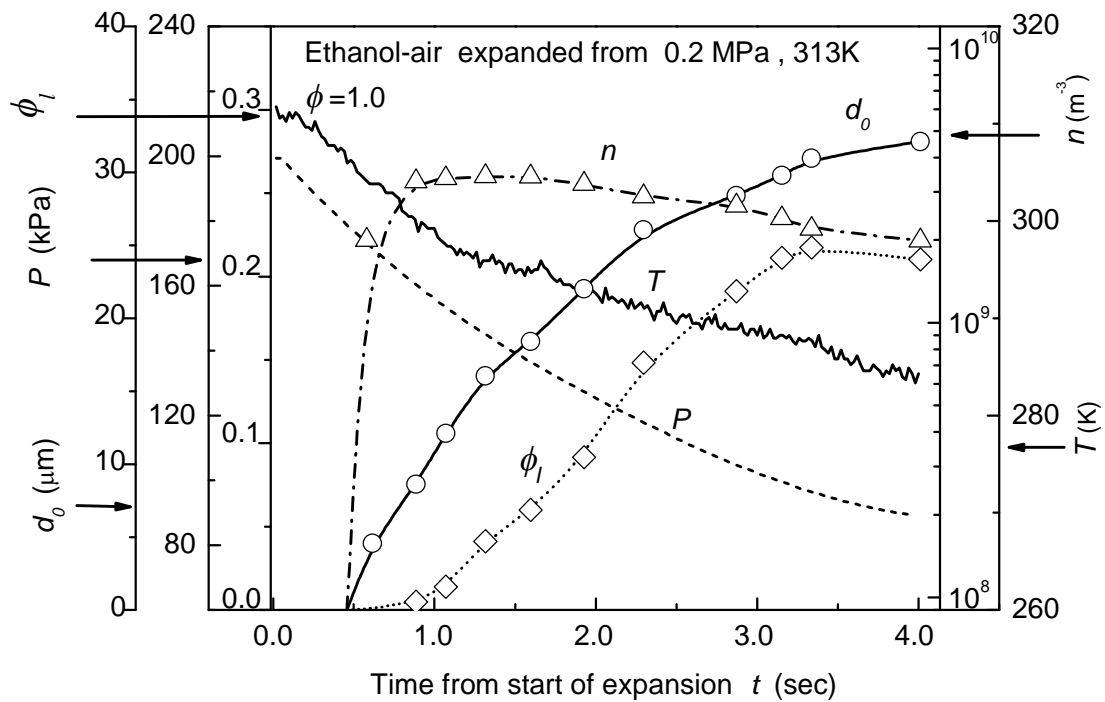


Figure 1. Typical variation of aerosol characterisation with the time for stoichiometric ethanol-air mixture expanded from 0.2 MPa, 313K.

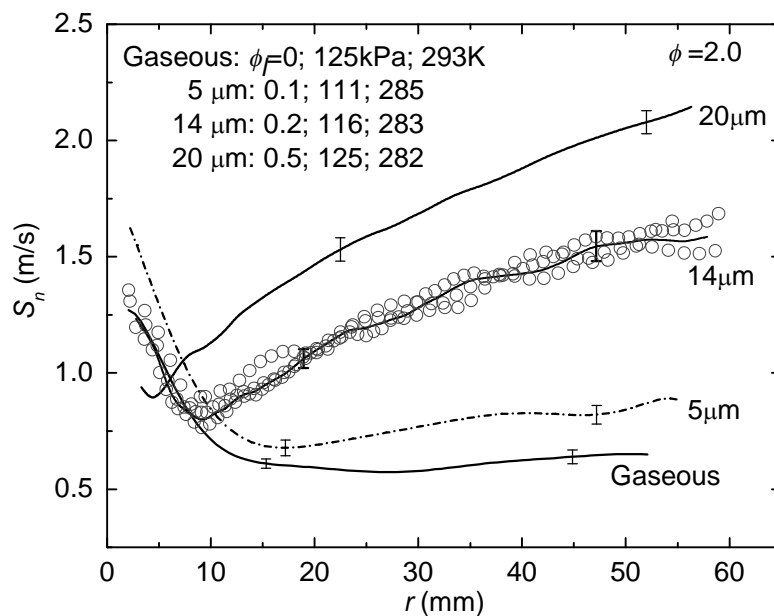


Figure 2. Variations of flame speeds at atmospheric pressure and temperature with radius for gaseous and aerosol *iso*-octane-air mixtures at $\phi = 2.0$, for different droplet diameters and liquid phase equivalence ratios, ϕ_l .

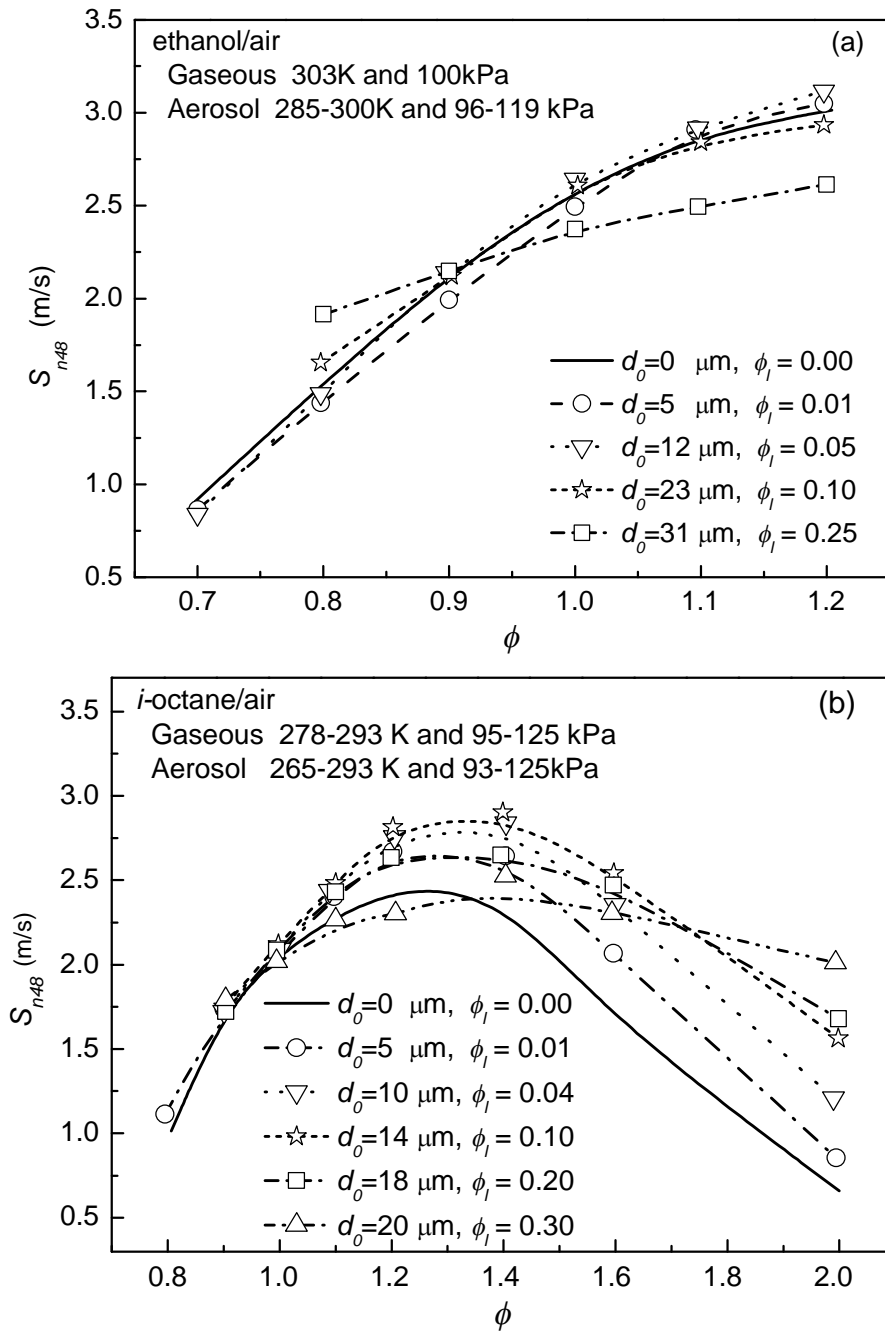


Figure 3. Flame propagating speeds of (a) ethanol/air and (b) *i*-octane/air flames at a radius of 48 mm, flames with various droplet sizes and liquid equivalence ratios.

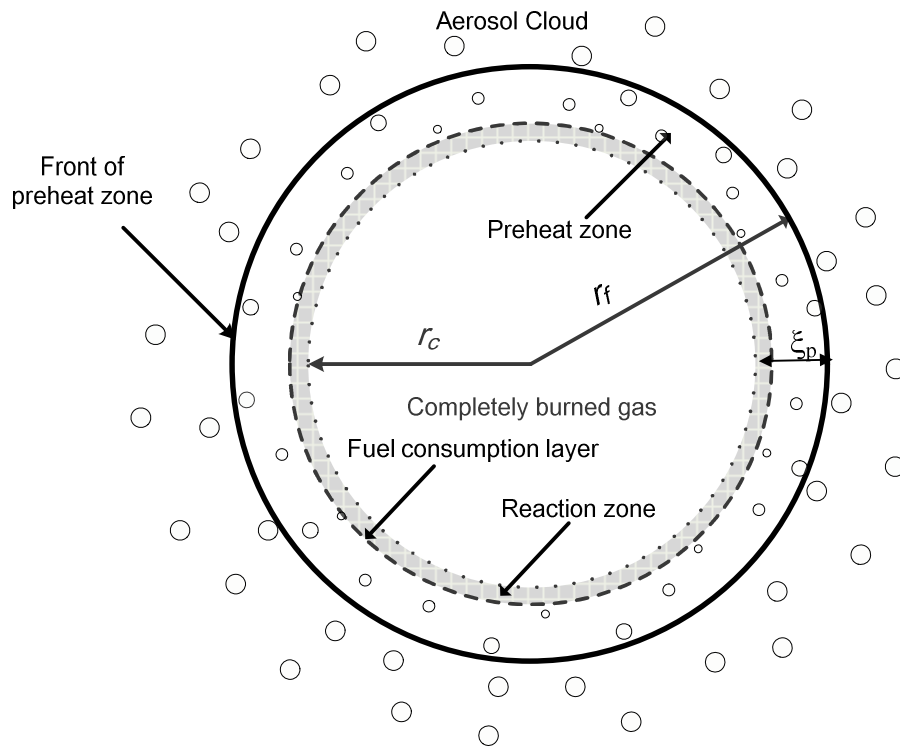


Figure 4. Spherically expanding aerosol flame configuration, with evaporation completed in the preheat zone.

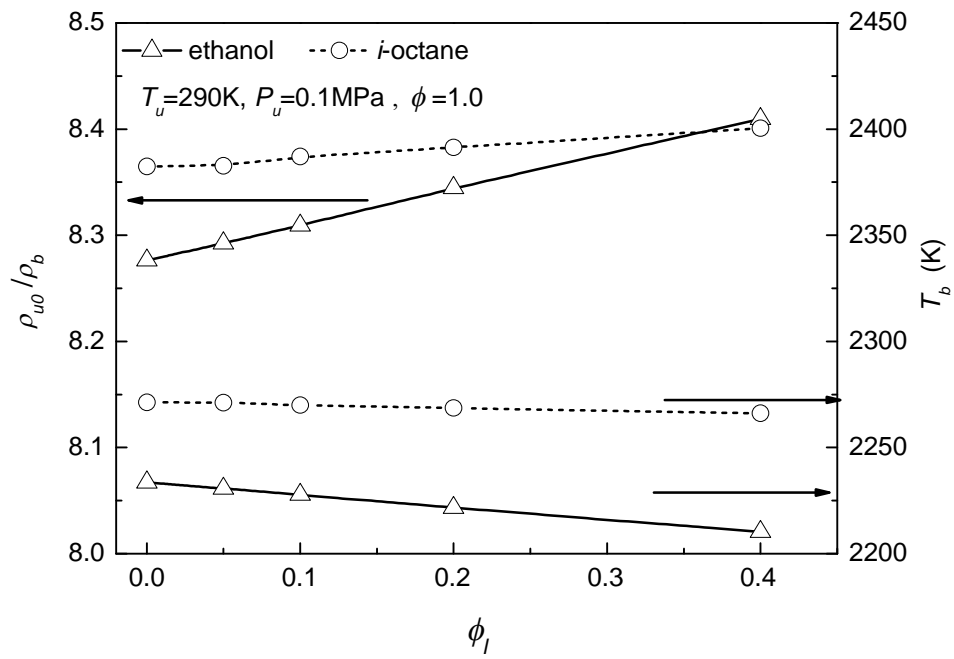


Figure 5. Variations, due to droplets, of burned gas temperature and ratio of densities for stoichiometric ethanol and *i*-octane aerosol mixtures.

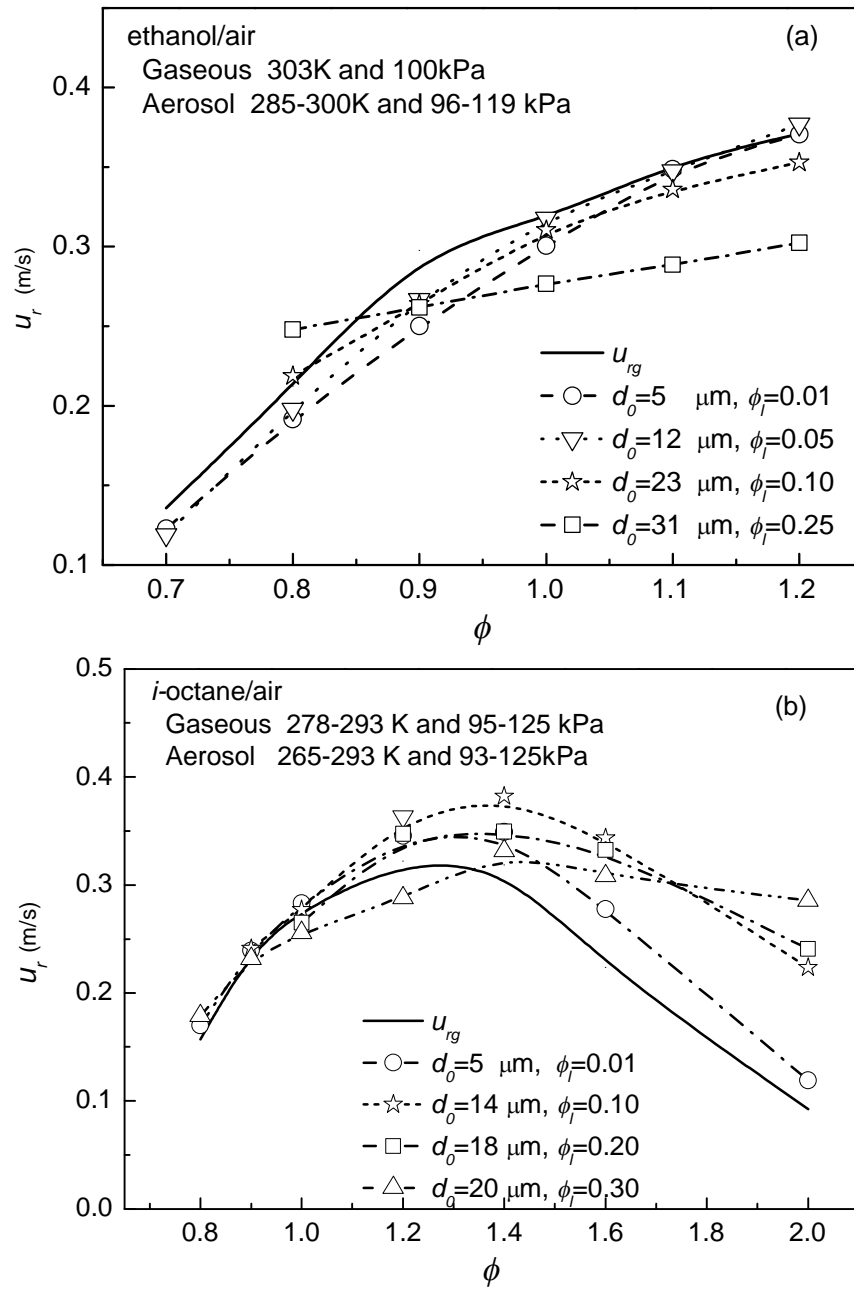


Figure 6. Mass burning velocities of (a) ethanol/air and (b) *i*-octane flames in air, at a radius of 48 mm with different droplet characteristics.

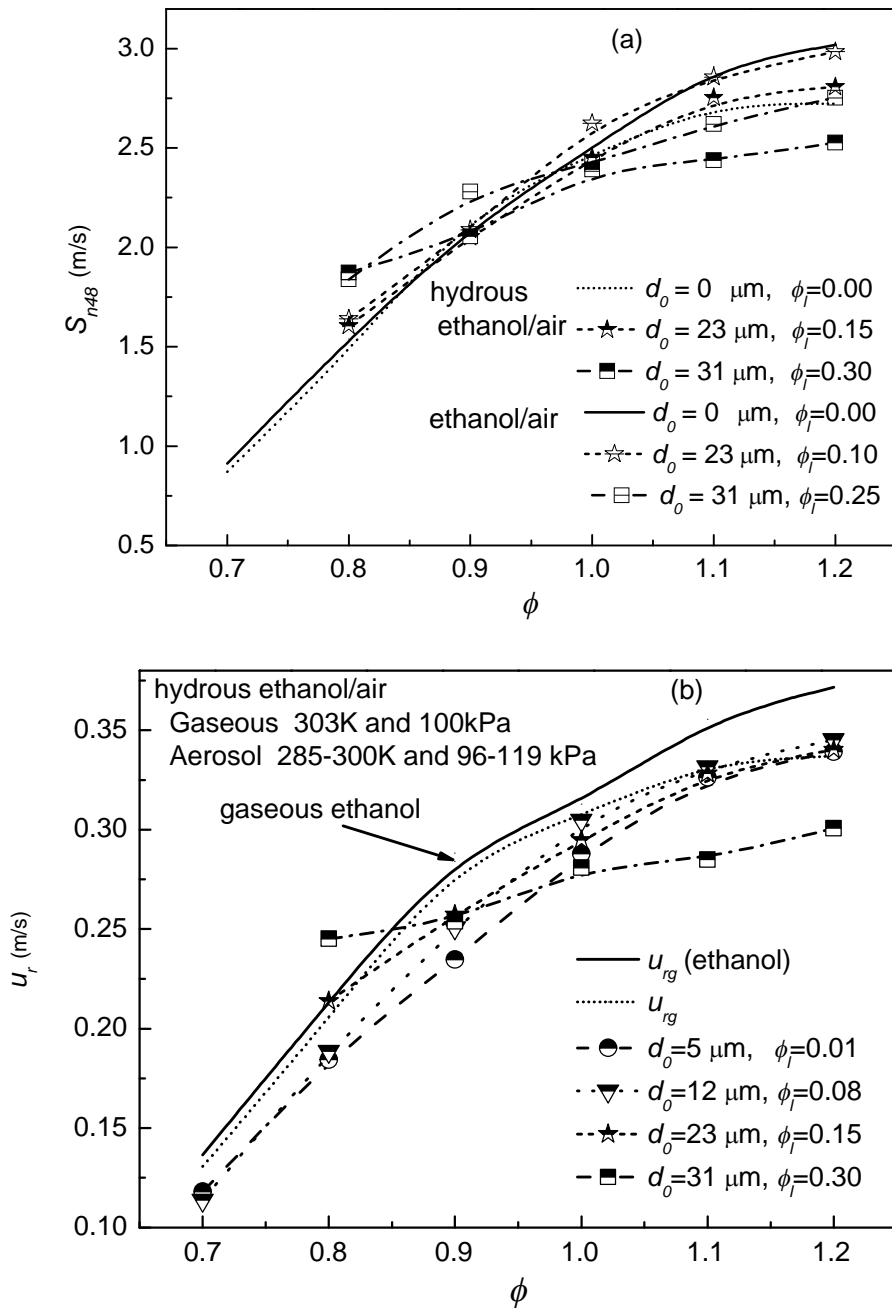


Figure 7. (a) Flame propagation speeds of hydrous ethanol/air and ethanol/air for different droplet characteristics. (b) Mass burning velocities of hydrous ethanol/air flames, at a radius of 48 mm with different droplet characteristics. Gaseous phase values on both (a) and (b).

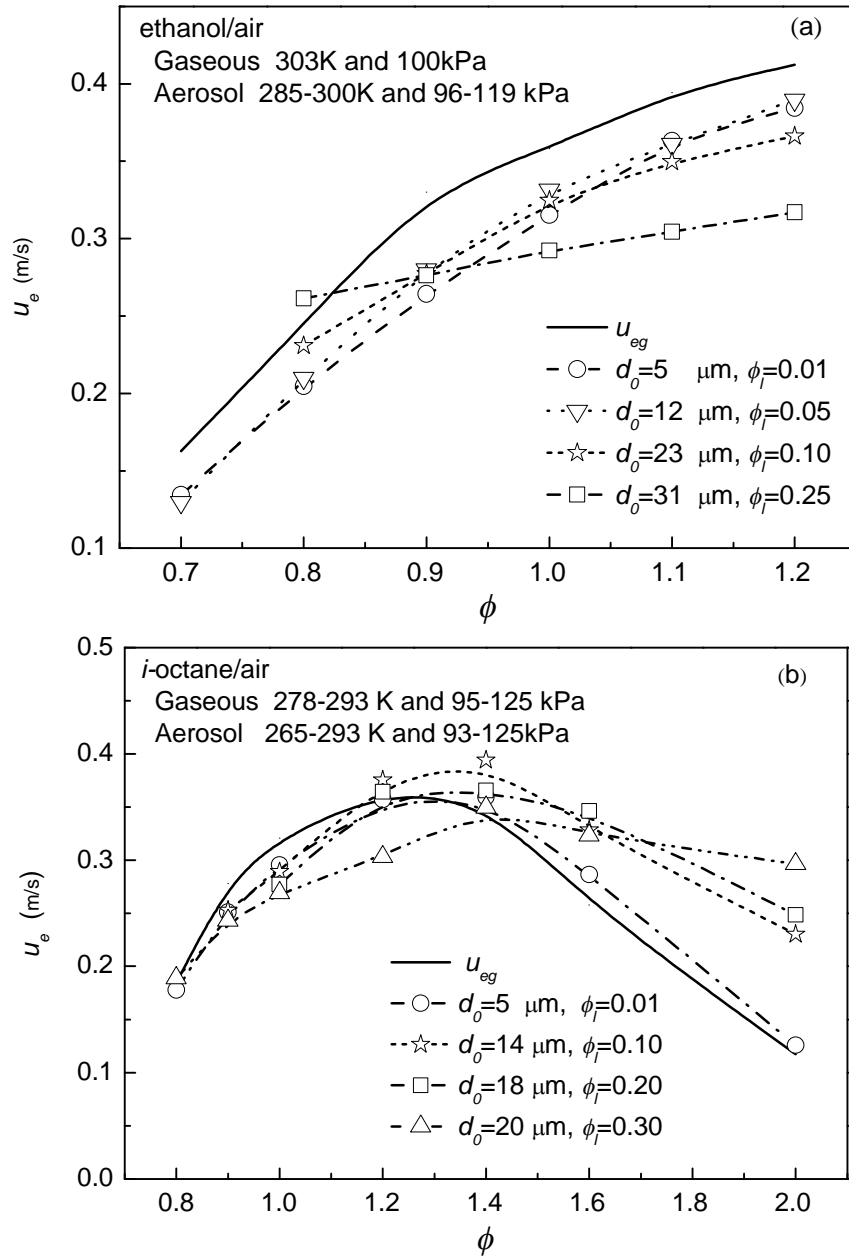


Figure 8. Entrainment velocities of ethanol and *i*-octane flames, at a radius of 48 mm with different droplet characteristics.

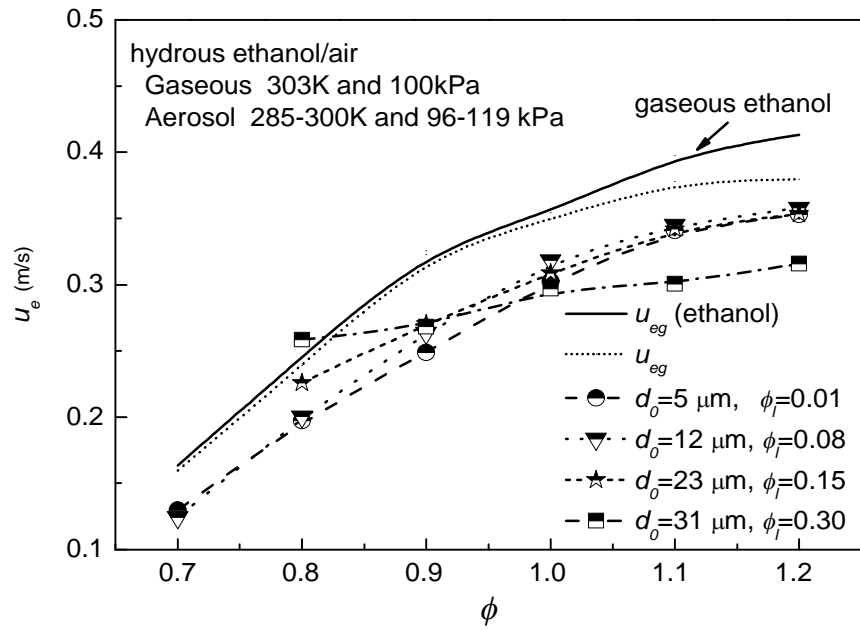


Figure 9 Entrainment velocities of hydrous ethanol/air flames, at a radius of 48 mm with different droplet characteristics.

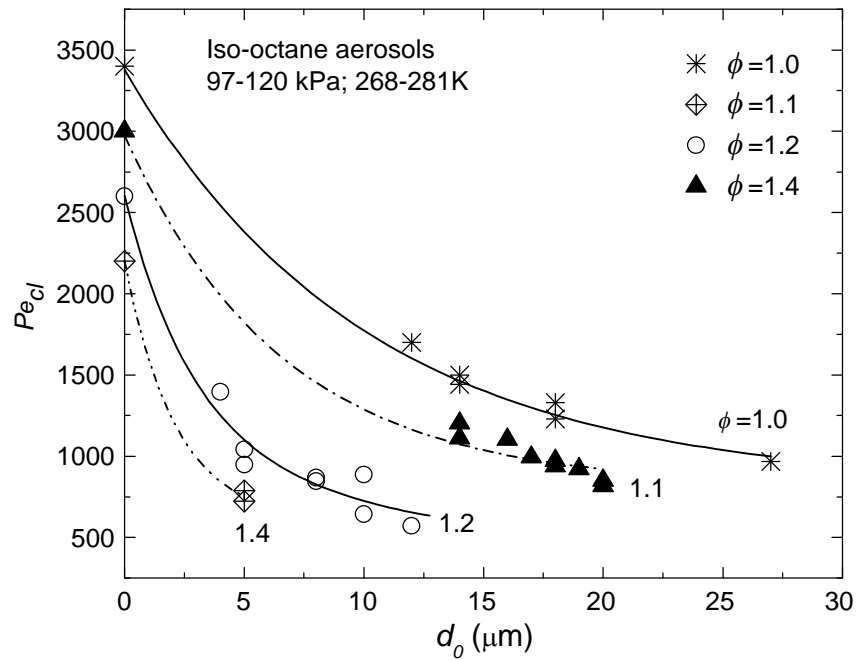


Figure 10. Variations of Pe_{cl} with d_o at different ϕ for *i*-octane/air aerosol flames.

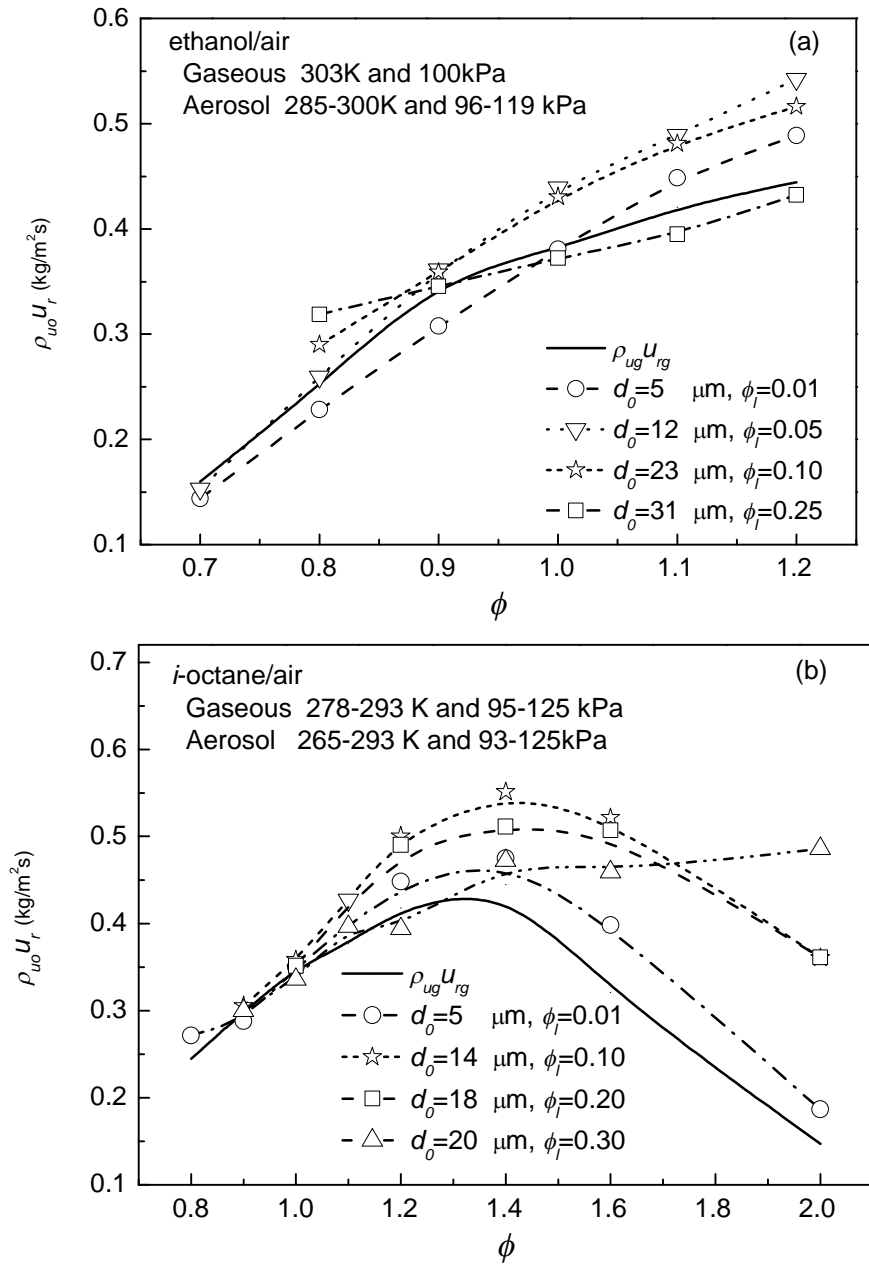


Figure 11. Mass burning fluxes of ethanol and *i*-octane/air flames with different droplet characteristics.

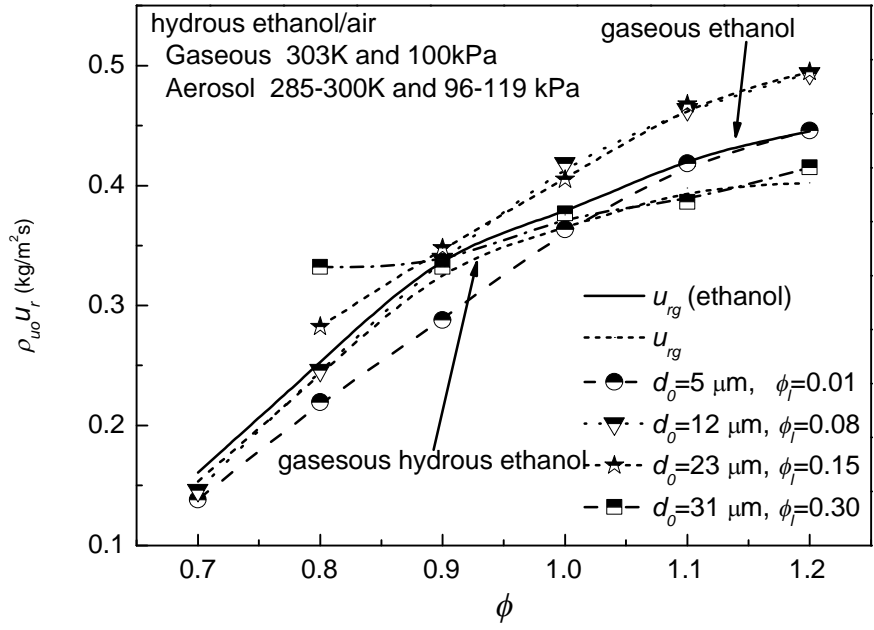


Figure 12. Mass burning fluxes of hydrous ethanol/air flames with different droplet characteristics.

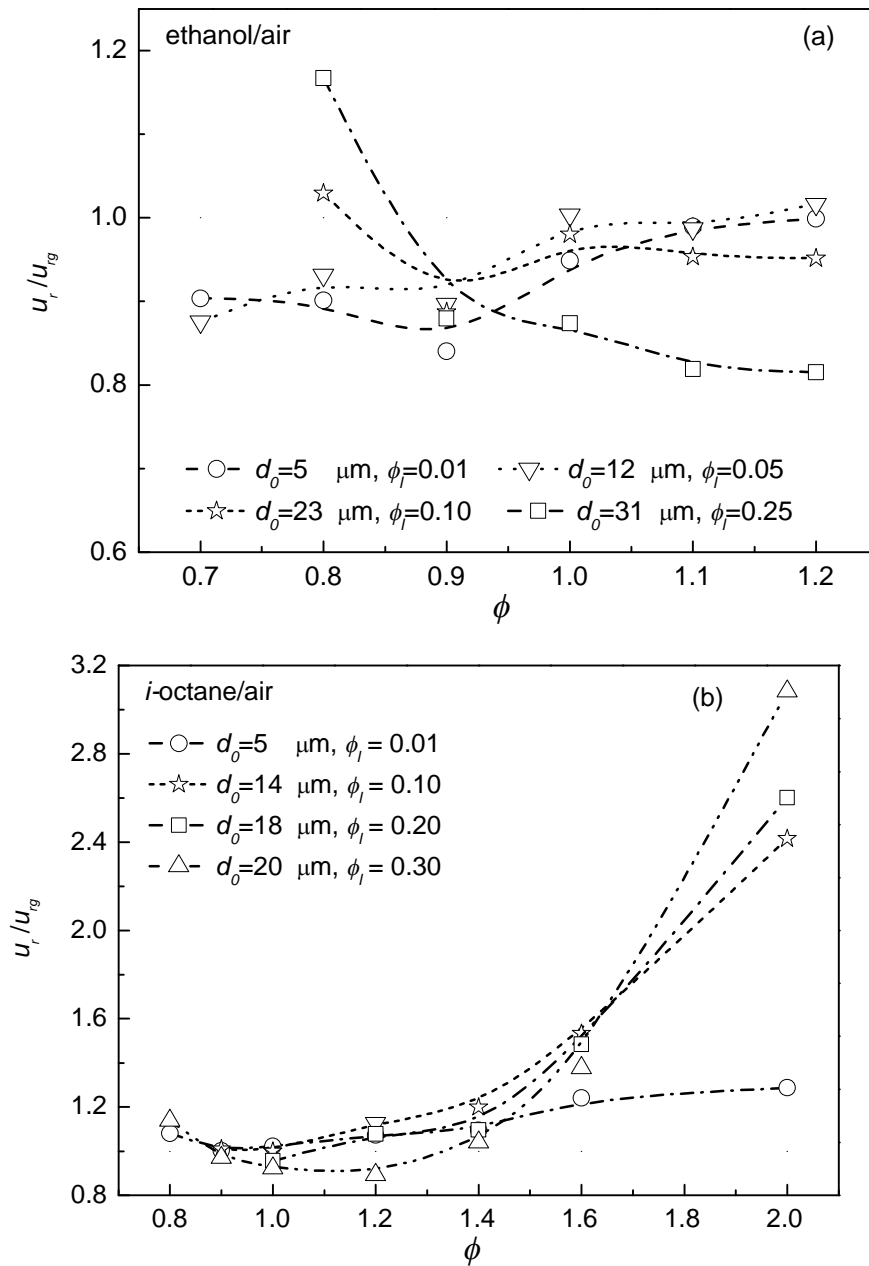


Figure 13. Normalised mass burning velocities of ethanol and *i*-octane/air flames, with different droplet characteristics.

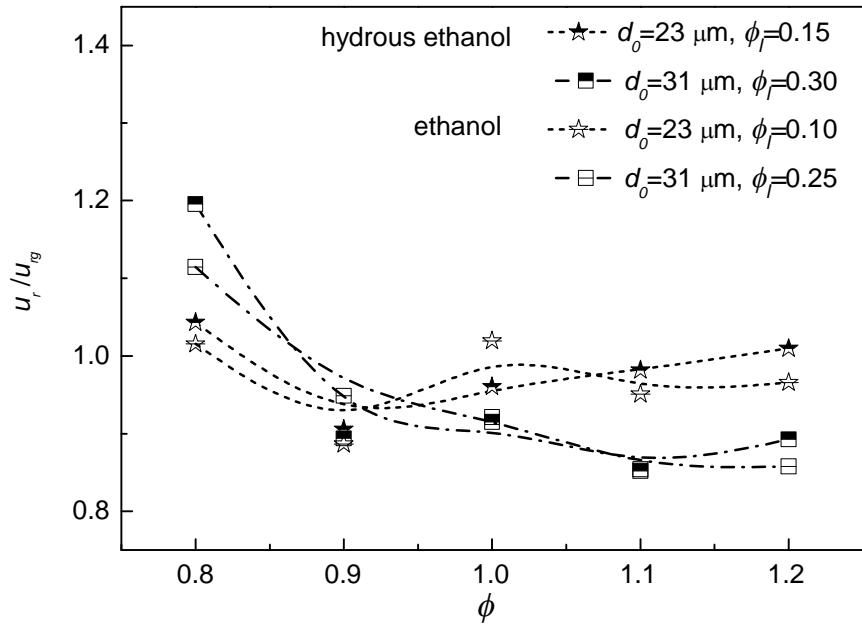


Figure 14. Normalised mass burning velocities of hydrous ethanol and ethanol/air flames, with different droplet characteristics.

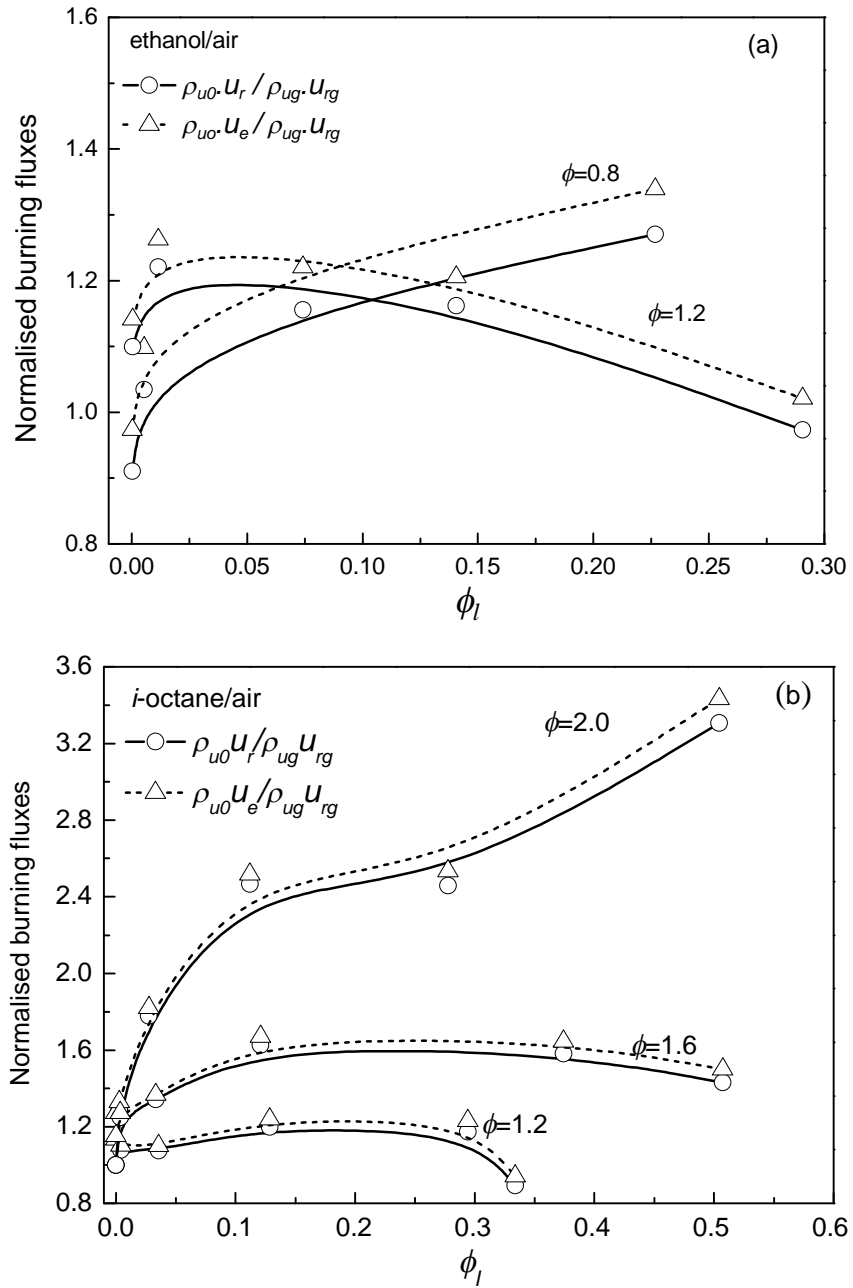


Figure 15. Effects of liquid equivalence ratio on mass burning and mass entrainment fluxes, normalised by the mass burning fluxes of the equivalent gaseous flames. The droplets diameters are 0, 5, 12, 23 and 31 μm for ethanol/air mixtures and 0, 5, 14, 18 and 20 μm for *i*-octane with increasing ϕ_l respectively.

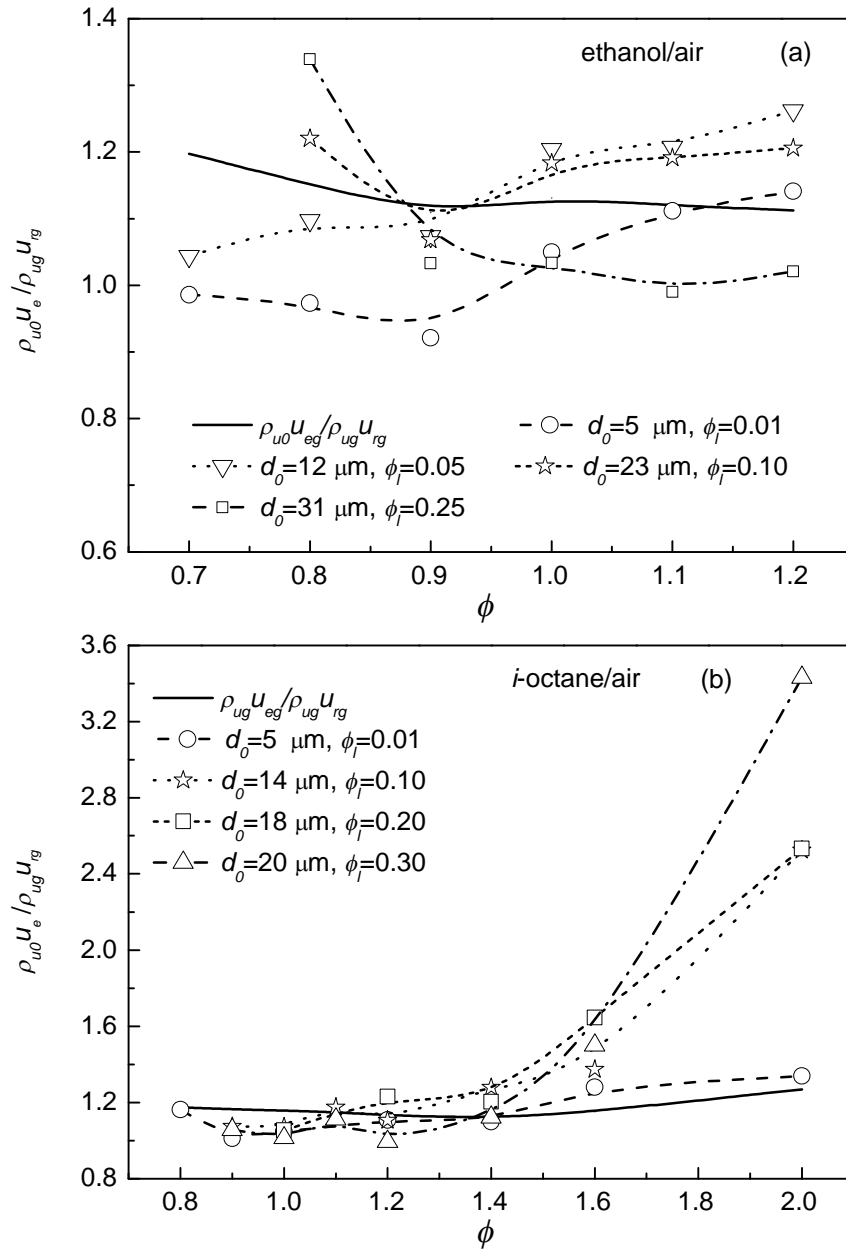


Figure 16. Normalised mass entrainment fluxes of ethanol/air and *i*-octane flames with different droplet characteristics.

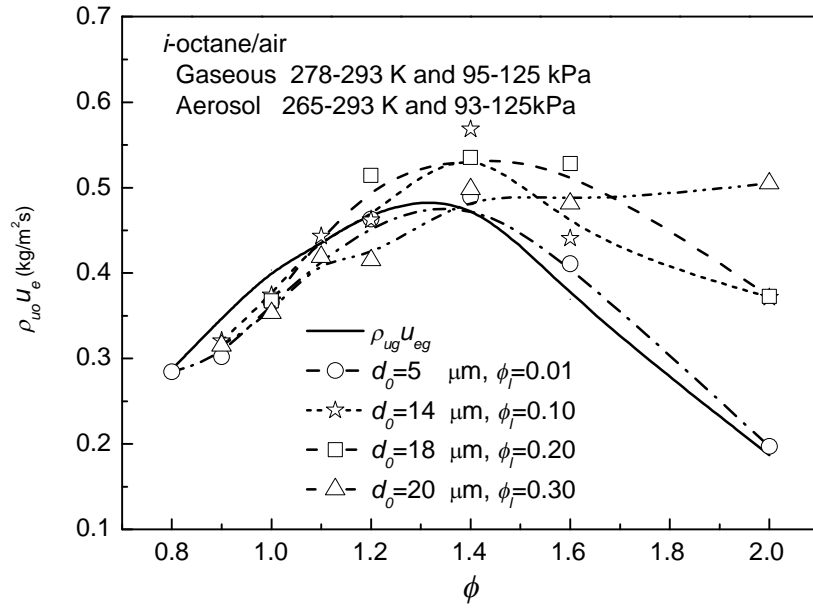


Figure 17. Mass entrainment fluxes of *i*-octane flames with different droplet characteristics.

APPENDIX: Evaporation of Droplets

The presented analysis is an attempt to identify those regimes in which near-complete evaporation might occur in the preheat zone, and those in which droplets might penetrate into the reaction zone. The rate of droplet evaporation is expressed by

$$\frac{d(d^2)}{dt} = -k, \quad (\text{A1})$$

where k is the evaporation rate constant for the mixture. Values of k depend upon the fuel gaseous thermal conductivity, specific heat, boiling point, and latent heat, as well as the surrounding temperature and pressure.

Table A1 shows some experimental and theoretical values of the evaporation rate constants, k , from [A1, A2, A3]. Hallett and Beauchamp [A3] measured ethanol evaporation at 703, 893 and 1023K, and proposed a model, which showed good agreements with their measurements. For *i*-octane, there is significant scattering in the measured and predicted values. The model proposed in [A2] gave lower values of k than those in [A4]. Since the thermal physical properties of *i*-octane are comparable to those of *n*-octane, it is assumed that the values of k for the two fuels would be close.

Values theoretically predicted by Mak [A1] were generally comparable with those predicted by Hubbard et al. [A5], and fairly close to the predictions of Ra and Reitz [A2]. All the available data on k at the different temperatures were considered. This revealed significant scatter, but best fits yielded exponential correlations of k with temperature for these two fuels. The correlation gave values of k at 400, 1000 and 1600K, respectively of 0.131, 0.411 and 1.284 mm²/s for ethanol, and of 0.143, 0.279 and 0.528 mm²/s for *i*-octane.

There are few data available on the evaporation of hydrous ethanol. With multi-component mixtures, evaporation may occur sequentially, from the lower boiling point to the higher one [A4]. The component with the lowest boiling temperature starts to evaporate when the droplet temperature reaches its boiling temperature. Each component evaporates separately, following the d^2 law. For azeotropic hydrous ethanol, the ethanol would evaporate first, followed by the small amount of water. Hence, values of k for hydrous ethanol, were assumed to be the same as those for pure ethanol over the same ranges of temperature.

Two sub-zones are identified within the preheat zone of thickness, ξ_p , the first being one in which there is a relatively slow rise in temperature from T_u to 450K. The latter temperature approximates that of the schlieren front that yielded the measured flame speeds, S_{n48} , in Figs. 3. Bradley et al. [A7] found that for premixed gaseous flames at atmospheric pressure:

$$r_f = r_{sch} + 1.95(v/u_\ell)(\rho_{ug}/\rho_b)^{0.5}, \quad (\text{A2})$$

where r_{sch} is the schlieren front radius and u_ℓ is the unstretched laminar burning velocity, and the bracketed term is the ratio of unburned to burned gas density. In the second part of the preheat zone the temperature gradient is near-constant from 450 to 1600K. This is followed by the fuel consumption layer, the thickness of which is about 0.1 of that of the preheat zone. For similar gaseous flames to those presently studied this is followed by rapid radical reactions in the reaction zone [A8]. The overall thickness of the preheat zone is between 6 and 7.4 times v/u_ℓ [A9] and a value of 6.7 was assumed.

A marching numerical integration of Eq. (A1) through the preheat zone enabled the changes in d^2 to be found at incremental times, given by the incremental distance in x divided by the values of entrainment velocity and k at the changing temperature T . Shown in Fig. A1 are some typical values of $(d/d_o)^3$ through the preheat zone for $d_o = 10$ and $31 \mu\text{m}$, in ethanol/air mixtures. Evaporation was complete for the smaller size and, where it was incomplete for the other conditions, the thickness of the pre-heat zone, ξ_p , is given.

The full and broken curves in Fig. 2A show calculated critical values of droplet diameter, d_{ocr} , at different ϕ for the two fuels, above which less than 90% of the droplet mass is evaporated in the pre-heat zone, $((d/d_o)^3 \geq 0.1)$. Previous studies suggest that when the droplets are evaporated in the preheat zone the flame speed is close to that of the corresponding gaseous pre-mixture. With this criterion, reference to the *ethanol/air* data in Fig. 3(a) suggests the upper limits for initial droplet size, d_{ocr} , for near complete evaporation at $\phi = 0.9, 1.0$ and 1.1 are about $26, 24$ and $23 \mu\text{m}$. For *i-octane/air*, Fig. 3(b) suggests that, for $\phi = 0.8, \text{ and } 0.9$ d_{ocr} is greater than $20 \mu\text{m}$ and for $\phi = 1.0, 1.1$ and 1.2 d_{ocr} is $20, 20$ and $19 \mu\text{m}$. These inferred values are shown by black-filled asterisks in Fig. A2 for ethanol/ait and unfilled asterisks for *i-octane/air*. For values of ϕ greater than 1.2 this procedure cannot be adopted due to the presence of the different instabilities, discussed in Section 6.

Table A1. Evaporation rate constants for ethanol, and *i*-octane, and *n*-octane.

Fuel	Evaporation rate constant, k (mm ² /s)	
	theoretically predicted	Measured
Ethanol	0.201 (573K), [A6] 0.383 (973K), [A3].	0.192 (703K), 0.321 (893K), 0.427 (1023K), [A3].
<i>i</i> -Octane	0.120 (500K), ; 0.252 (1000K), [A2]	0.25 (623K), 0.310 (823K), 0.431 (1000K), [A4].
<i>n</i> -Octane	0.212 (573K), [A6]; 0.137 (600K), 0.319 (1200K) [A5]	0.290 (973K), [A1]

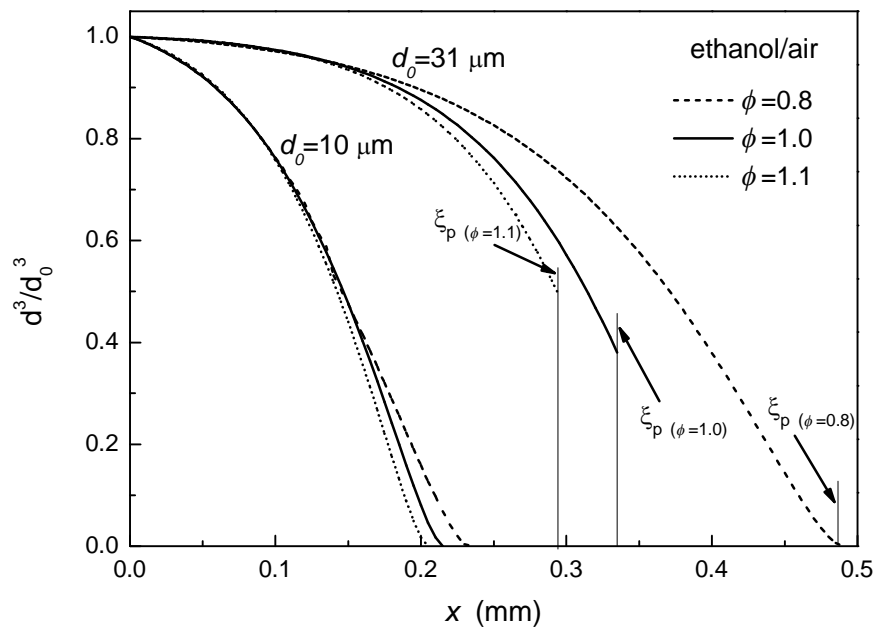


Figure A1 Some calculated changing droplet diameters due to evaporation in preheat zone, thickness, ξ_p , for ethanol/air mixtures.

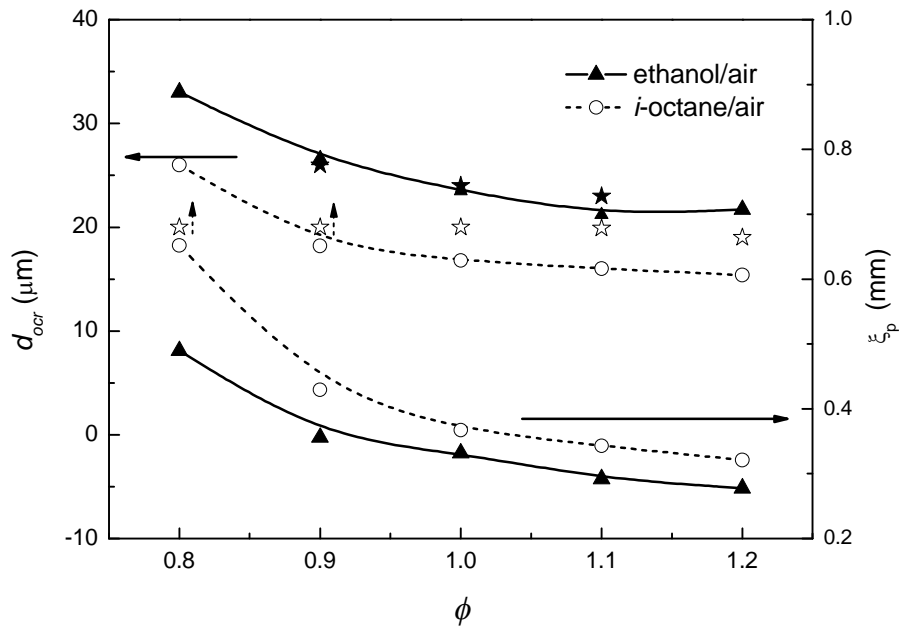


Figure A2. Critical initial droplet diameters, d_{ocr} , for 90% evaporation in preheat zone, thickness ξ_p , at different ϕ for ethanol/air and *i*-octane/air. Asterisks suggest values given by flame speeds.

References

- A1. R. Mak, (1979) "Fundamentals of droplet ignition", Ph. D. Thesis, Mechanical Engineering Department, University of Leeds, Leeds, UK.
- A2. Y. Ra, R.D. Reitz, (2003) *International Journal of Engine Research* 4, 193-218.
- A3. W.L.H. Hallett, S. Beauchamp-Kiss, (2010) *Fuel* 89, 2496–2504.
- A4. S.S. Chung, O. Kawaguchi, (1995) *JSME Series B* 38 (1), 121-128
- A5. G.L. Hubbard, V.E. Denny. A.F. Mills, (1975) *Int. J. Heat Mass Transfer* 18, 1003-1008.
- A6. S. Kotake, T. Okazaki, (1969) *Int. J. Heat Mass Transfer* 12, 195-609.
- A7. D. Bradley, P.H. Gaskell, X.J. Gu, (1996) *Combust. Flame* 104, 176-198.
- A8. N. Peters, F.A. Williams, (1987) *Combust. Flame* 68, 185-207.
- A9. S.H. Chung, D.H.Chung,C. Fu, P.Cho (1995), *Proc. Seminar on Combustion Phenomena in I.C. Engine*, Seoul, p. 29.s

Acknowledgement

The authors are pleased to acknowledge the financial support of the National Natural Science Foundation of China (No. 51076167) for S.Y. Liao.